MODELING DIE SWELL OF SECOND-ORDER FLUIDS USING SMOOTHED PARTICLE HYDRODYNAMICS

By
SAMIR HASSAN SADEK

Submitted to Graduate School of Engineering and Natural Sciences
In Partial Fulfillment of
The Requirements for the Degree of
Master of Science

Sabanci University
January 2010

MODELING DIE SWELL OF SECOND-ORDER FLUIDS USING SMOOTHED PARTICLE HYDRODYNAMICS

APPROVED BY:

Assistant Prof. Mehmet Yildiz ……..
(Thesis supervisor)

Assistant Prof. Ali Koşar ……..
(Thesis Co- Advisor)

Prof.Dr. Ali Rana Atilgan ……..

Associate Prof. Mustafa Unel ……..

Associate Prof. Serhat Yesilyurt ……..

DATE OF APPROVAL: ……

MODELING DIE SWELL OF SECOND-ORDER FLUIDS USING SMOOTHED PARTICLE HYDRODYNAMICS

SAMIR HASSAN SADEK

ME, M.Sc. Thesis, 2010

Thesis supervisor: Assistant Prof. Mehmet Yildiz

Thesis Co- Advisor: Assistant Prof. Ali Koşar

Key Words: Smoothed particle hydrodynamics (SPH); free surface flow; die swell; extrudate swell; non-newtonian fluids; second-order fluids; incompressible SPH; weakly compressible SPH.

Abstract

This work presents the development of both weakly compressible and incompressible Smoothed Particle Hydrodynamics (SPH) models for simulating two-dimensional transient viscoelastic free surface flow which has extensive applications in polymer processing industries. As an illustration with industrial significance, we have chosen to model the extrudate swell of a second-order polymeric fluid. The extrudate or die swell is a phenomenon that takes place during the extrusion of polymeric fluids. When a polymeric fluid is forced through a die to give a polymer its desired shape, due to its viscoelastic non-Newtonian nature, it shows a tendency to swell or contract at the die exit depending on its rheological parameters. The die swell phenomenon is a typical example of a free surface problem where the free surface is formed at the die exit after the polymeric fluid has been extruded. The swelling process leads to an undesired increase in the dimensions of the extrudate. To be able to obtain a near-net shape product, the flow in the extrusion process should be well-understood to shed some light on the important process parameters behind the swelling phenomenon. To this end, a systematic study has been carried out to compare constitutive models proposed in literature for second-order fluids in terms of their ability to capture the physics behind the swelling

phenomenon. The effects of various process and rheological parameters on the die swell such as the extrusion velocity, normal stress coefficients, and Reynolds and Deborah numbers have also been investigated. The models developed here can predict both swelling and contraction of the extrudate successfully. The die swell problem was solved for a wide range of Deborah numbers and for two different Re numbers. The numerical model was validated through the solution of fully developed Newtonian and Non-Newtonian viscoelastic flows in a two-dimensional channel, and the results of these two benchmark problems were compared with analytic solutions, and good agreements were obtained.

İKİNCİ DERECEDEN AKIŞKANLARDA KALIP ŞİŞMESİ OLAYININ DÜZLEŞTİRİLMİŞ PARTİKÜL HİDRODİNAMİĞİ İLE MODELLENMESİ

SAMİR HASSAN SADEK

ME, M.Sc. Thesis, 2010

Thesis supervisor: Assistant Prof. Mehmet Yildiz

Thesis Co- Advisor: Assistant Prof. Ali Koşar

Anahtar Kelimeler: Düzleştirilmiş partikül hidrodinamiği; serbest yüzey akışı; kalıp şişmesi; ekstrüde malzeme şişmesi; Newtonian olmayan akışkanlar; ikinci dereceden akışkanlar; sıkıştırılamaz düzleştirilmiş partikül hidrodinamiği; kısmi sıkıştırılabilir düzleştirilmiş partikül hidrodinamiği

Özet

Bu projede polimer imalatı endüstrisinde kapsamlı uygulamalara sahip iki boyutlu zamana bağımlı viskoelastik serbest yüzey akışı, sıkıştırılamaz ve kısmi sıkıştırılabilir düzleştirilmiş partikül hidrodinamiği yaklaşımı kullanılarak modellenmiştir . Endüstriyel açıdan önemi göz önünde bulundurularak ikinci dereceden polimerik akışkanların ekstrüzyon şişmesinin modellenmesine karar verilmiştir. Kalıp şişmesi (ekstrüde malzeme şişmesi) olayı polimerik akışkanın ekstrüzyonu esnasında gözlemlenmektedir. Polimerik akışkan istenilen boyutlarda şekillendirmek amacıyla kalıba basıldığında, akışkanın viskoelastik Newtonian olmayan yapısından dolayı akışkan kalıp çıkışı esnasında şişme yada büzülme eğilimi gösterir. Kalıp şişmesi olayı tipik bir serbest yüzey problemi örneğidir. Serbest yüzey polimerik akışkanın kalıptan çıkması sonucu oluşan yüzeydir. Bu şişme olayı ekstrüde malzemenin boyutlarında istenilmeyen artışlara yol açar. İstenilen boyutlara sahip bir ürün elde edebilmek için ekstrüzyon işlemi esnasındaki akışın iyi anlaşılması gerekmektedir. Böylelikle şişme olayının ardında olan önemli işlem parametrelerine ışık tutulacaktır. Bu bağlamda, literatüre ikinci

dereceden akışkanlar için kullanılan bünye denklemlerinin şişme olayının ardındaki fiziği yakalayıp yakalayamayacaklarını tespit etmek için sistematik bir araştırma gerçekleştirilmiştir. Ayrıca, kalıp şişmesi olayına ekstrüzyon hızının, normal stres katsayılarının, reolojik parametrelerin ve Reynolds ve Deborah sayılarının etkisi incelenmiştir. Geliştirilen model esktrüde malzemenin şişme yada büzülme eğilimi başarılı bir şekilde tespit edebilmektedir. Kalıp şişmesi problemi farklı Deborah sayıları ve iki farklı Reynold sayısı için çözülmüştür. Numerik model, iki boyutlu bir kanalda tam gelişmiş Newtonian ve Non-Newtonian viskoelastik akışların çözümlenmesi yapılarak doğrulamıştır. Bu iki test probleminin sonuçları analitik çözümler ile kıyaslanmış ve analitik çözümlerle iyi bir uyum elde edilmiştir.

Acknowledgements

I am heartily thankful to my supervisor Dr. Mehmet Yildiz who provided encouragement and guidance during the completion of this work. It is an honor for me to be one of his students. I confess that by working with him, I gained significant amount of valuable knowledge and experience in the field of computational fluid mechanics and polymer processing which will help me progress in my carrier effectively and productively. I am grateful that I was given a chance to do cutting edge research on a new meshless Lagrangian computational method. I would like to extend my sincere thanks to my thesis Jury member's Dr. Atılgan, Dr. Koşar, Dr. Mısıroğlu, Dr. Ünel, Dr. Yeşilyurt for their valuable time and constructive comments, which improved the quality of the current work significantly.

I would like to express my thanks and appreciation to my family in Egypt for their support, advice, motivation and patience during my stay in Turkey. I also extend my thanks to all Sabanci University members, whom I met during my study, and also to my friends.

I am grateful to the team of Erasmus Mundus ECW (Lot 2) project in Brussels, that gave me the opportunity to pursue my MSc. degree abroad. This opportunity will have a great resonance on my academic work in the future. Also, I would like to thank Erasmus for covering the expenses of my whole studying period for my MSc. degree at Sabanci University.

Lastly, I offer my regards and blessings to all of those who supported me in any respect during the completion my MSc. degree.

Table of contents

List of Figures

List of Tables

List of Abbreviation

c	Speed of sound
m	Particle mass
p	absolute pressure
$\vec{\mathbf{v}}$	Divergence-free fluid velocity
$\vec{\mathbf{f}}^{B}$	Body force
$\underline{\underline{\mathbf{I}}}$	Identity tensor
$\underline{\underline{\mathbf{T}}}$	Viscoelastic stress tensor
$\underline{\underline{\mathbf{A}}}$, A_{ij}	Deformation rate tensor
$\underline{\underline{\widehat{\mathbf{A}}}}$	Kinematic tensor
$\vec{\mathbf{e}}_k$	Base vector
h_{ij}	Average smoothing length
$v_{\max}$	Maximum flow velocity
$W(r_{\mathbf{ij}}, h)$	Smoothing kernel function
L_o	Characteristic length
N_1	First normal stress differences
N_2	Second normal stress differences
$\left\|\vec{\mathbf{r}}_{\mathbf{ij}}\right\|$, $\mathbf{r_{ij}}$	Magnitude of the distance vector
$t_{process}$	Characteristic process time.
f	Refer to a function
d	Problem dimension
$\vec{\mathbf{n}}$	Unit normal to the discontinuity surface
$n_{\mathbf{i}}$	Number density
M	Mach number
De	Deborah number
Re	Reynolds number
CFL	Courant-Friedrichs-Lewy condition
CEF	Criminale–Ericksen–Filbey constitutive relations
SPH	Smoothed Particle Hydrodynamics
ISPH	Incompressible smoothed particle hydrodynamics
WSPH	weakly compressible smoothed particle hydrodynamics
D / Dt	Material time derivative
$\mathfrak{D}$ / $\mathfrak{D}t$	Convected time derivative operator

Greek Symbols

ρ	Particle density
ρ_0	Initial Particle density
μ	Kinematic viscosity

υ	Dynamic viscosity
$\underline{\underline{\boldsymbol{\sigma}}}$	Total stress tensor
$\underline{\underline{\boldsymbol{\tau}}}$	Viscous components of the viscoelastic stress tensor
$\underline{\underline{\boldsymbol{\varepsilon}}}$	Elastic components of the viscoelastic stress tensor
α_1	First normal stress coefficients
α_2	Second normal stress coefficients
$\underline{\underline{\omega}}$, ω_{ij}	Vorticity tensor
λ	Material relaxation time
δ^{kl}	Kronecker delta
δ	The relative incompressibility or the density variation factor
γ	Surface tension
Γ	Mean curvature
$\nabla()$	Gradient operator
$\nabla\bullet()$	Divergent operator
∇^2	Laplacian operator
$\nabla_{(s)}$	Surface gradient operator
$\sum$	Summation operator
Δt	Time increment
$v_{i,j}$, $v_{j,i}$	Velocity gradient tensor
φ	Problem dependent coefficient
κ	Coefficient associated with the particular kernel function
$\langle\ \rangle$	Denotes the kernel approximation
$\llbracket\ \rrbracket$	The jump of the enclosed quantities across the discontinuity surface

Superscripts

n	Old time step value
$(n+1)/2$	Half time step value
$(n+1)$	Corrected time step value
*	Temporary field variables

Subscripts

i	Refer to Particle of interest
j	Refer to Neighboring particle
ij	Values between particle i and j

CHAPTER 1

1 INTRODUCTION

1.1 Motivation

Polymeric materials have long been used for a variety of applications in our daily lives in the forms of rods, tubes and sheets. Most of these products are manufactured by extruding molten polymers (hereafter also referred to as a polymeric fluid, or liquid) through a die. In general, there are many steps in the manufacturing of polymeric products with desired shape and dimensions. These fabrication steps play a very important role in determining the quality of final products. The fabrication process starts with the synthesis of raw materials and ends with the manufacturing of finished products. The last processing step includes the extrusion of a polymeric fluid through a die. The extruded polymeric fluid exhibits viscoelastic characteristics because of the existence of normal stresses that can distort the cross section of the extrudate. The deformation of the polymeric liquid outside the die is widely referred to as the extrudate or die swell. The die swell phenomenon leads to a change in product's final shape, thereby hindering the effective control of the cross section of the final product. The extrudate swell is highly sensitive to rheological properties of polymers (whether being a Newtonian or a non-Newtonian) and also the processing variables such as flow rate and temperature. Die swell is defined as the ratio of the extrudate diameter to the die exit diameter [1].

To improve both the quality of the polymeric final products and the productivity of the fabrication process require a good understanding of rheological behavior of polymeric liquids,

especially understanding the die swell phenomenon for controlling or reducing its undesired effect. This highly non-linear and complex problem has been the subject of extensive research in the last few years. Towards this end, considerable effort has been dedicated towards predicting the behavior of the viscoelastic polymeric fluids using either experimental techniques [1, 2] or numerical approaches. Numerical approaches reported in literature to model the die swell behavior include the finite element method [3-6], and finite difference technique [7] based on the marker and the cell philosophy [8, 9]. Early works on the die swell can be classified into two- and three- dimensional models with various forms of die geometries such as two-dimensional convergent, divergent or half converging/ half tubular channels [3, 4, 6, 8-10], and three-dimensional circular, square or varied cross-section channels [5, 11]. These reported studies have shown that the die swell is influenced by the rheological characteristic of polymeric fluids such as the sign and the value of first and second normal stress coefficients [6], process parameters such as the extrusion velocity [9] and the geometry of the die [1].

In all the previously reported computational studies, the die swell process has been modeled using mesh-dependent approaches. When tackling problems that involve complex free surfaces, splashing, and fluid-solid interactions, mesh dependent techniques, due to their Eulerian nature, require the solution of additional sets of equations for tracking free surface, and may necessitate the re-meshing of computational grid in regions where large mesh-deformation and fracture may occur. Hence, modeling these types of flow problems with mesh dependent methods presents significant challenges in computational fluid dynamics. Within the last two decades, meshless methods have started appearing in the field of computational fluid mechanics field as complementary methods to deal specifically with problems as described above. Smoothed particle hydrodynamics (SPH) is one of the techniques in meshless Lagrangian particle methods used to solve partial differential equations. Although originally proposed to handle cosmological simulations [12], the SPH technique has become increasingly generalized to handle many types of fluid and solid mechanics problems such as heat transfer [13], multiphase flow [14], solidification [15], crystal growth [16], dynamic response of elasto-plastic materials [17], free surface flows [18-20], and low-Reynolds number viscous flows [21]. Owing to its Lagrangian nature, the SPH technique offers noticeable advantages for modeling such flows in comparison to mesh-dependent methods. SPH

advantages also include relatively ease of modeling complex material surface behavior, as well as relatively simple implementation of more complicated physics, such as non-Newtonian viscoelastic flows with and without free surface.

The SPH method has recently been extended to modeling non-Newtonian viscoelastic flows. The first attempt came with the work of Ellero et.al. [22] in which a corotational Jaumann–Maxwell model was employed for studying the viscoelastic relaxation in a two-dimensional channel. The same first author also studied the transient flow between the parallel plates for both Oldroyd- B and upper-convected-Maxwell fluids at low Reynolds numbers[23]. SPH method has also recently been used to model non-Newtonian flows with free surfaces. Shao et al. [18] simulated a dam breaking problem with a modified version of cross-model. Fang et al. [19] studied the impact of a drop of an Oldroyd-B fluid on a rigid plate using a weakly incompressible SPH approach. Rafiee et al. [24] has also recently modeled the impact of a drop and jet buckling of Maxwell and Oldroyd-B fluids with incompressible SPH approach.

The motivation behind this work is to scrutinize the feasibility and effectiveness of the SPH method to capture the important physics behind the die swell phenomenon, which is a real industrial application of a free surface problem. In this work, the polymeric fluid is treated as a second-order viscoelastic non-Newtonian liquid. To our best knowledge, the extrudate swell problem has been solved neither using SPH nor using any other meshless methods. Therefore, this work is a novel contribution to the field.

1.2 Thesis Outline

The scope of this thesis work covers modeling studies in polymer processing with a new meshless computational approach that has been applied to the study of the extrudate swell phenomenon in an extrusion process. Following a brief introduction of the subject, we have introduced the balance of mass and linear momentum as governing equations of the problem in hand along with various viscoelastic constitutive models in Chapter 2. In Chapter 3, the SPH method is presented together with the SPH discretization scheme for linearizing

governing equations and the solution algorithms for both WSPH, and ISPH approaches. In Chapter 4, the model problem together with its boundary conditions is outlined. Two benchmark problems are solved to validate the SPH model developed here. As well, we have discussed the outcomes of the modelling studies in detail referring to the effect of various process and rheological parameters on the die swell. The thesis work concludes with some remarks on the developed method and summarizes important findings of the current work as well as presents the future work in Chapter 5.

CHAPTER 2

2 DIE SWELL

2.1 Problem Definition

In polymer industry, one of the processes used for shaping or forming a polymeric product is extrusion where a polymeric liquid is forced through a die to give the polymer its desired shape. Most of the polymeric fluids behave as a viscous elastic fluid that has the ability to swell outside from the die exit when extruded. The swelling phenomena occurring at the die exit leads to an increase in the dimensions of the extruded fluid. Therefore, the final size of the product becomes greater than the geometrical dimensions of the die as simulated in Figure 2-1. The swelling phenomenon is a typical example for a free surface problem with boundaries moving and deforming in time. In the extrusion process, the free surface forms at the die exit after the polymeric fluid has been extruded through the die. For the sake of the readability of the thesis work, here we have introduced the die swell problem briefly. The more detailed problem description is provided in Chapter-4.

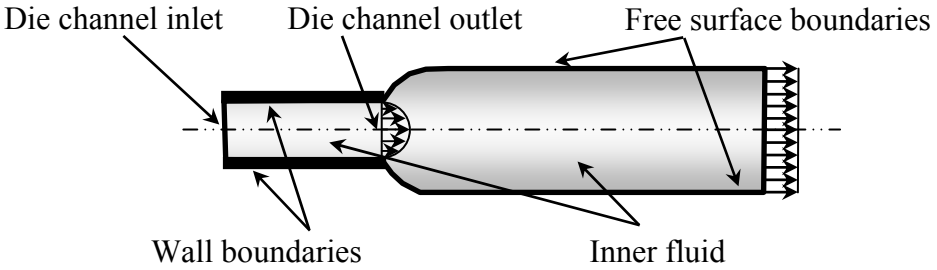

Figure 2-1: Die swell phenomena.

2.2 Governing Equations

The polymeric fluid is assumed to be a viscous incompressible non-Newtonian second-order fluid with negligible thermal effects (i.e. isothermal flow). The governing equations used to solve the fluid problems in this work are the mass and linear momentum balance equations which are expressed in the Lagrangian form and given in direct notation as

$$D\rho / Dt = -\rho \nabla \bullet \vec{\mathbf{v}}, \qquad \rho D\vec{\mathbf{v}} / Dt = \nabla \bullet \underline{\underline{\boldsymbol{\sigma}}} + \rho \vec{\mathbf{f}}^{B} \tag{2.1}$$

The incompressibility condition requires that the divergence of the fluid velocity $\nabla \bullet \vec{\mathbf{v}} = 0$ be zero. Here, ρ is the fluid density, $\vec{\mathbf{v}}$ is the divergence-free fluid velocity, $\underline{\underline{\boldsymbol{\sigma}}}$ is the total stress tensor, and $\vec{\mathbf{f}}^{B}$ is the body force term, respectively. The total stress is defined as $\underline{\underline{\boldsymbol{\sigma}}} = -p\underline{\underline{\mathbf{I}}} + \underline{\underline{\mathbf{T}}}$, where p is the absolute pressure, $\underline{\underline{\mathbf{I}}}$ is the identity tensor, $\underline{\underline{\mathbf{T}}}$ is the viscoelastic stress tensor. Finally, D / Dt is the material time derivative operator defined as $D / Dt = \partial / \partial t + v_l \partial / \partial x_l$

2.3 Constitutive Equations

In the literature related to the die swell modelling or the second-order fluid in general, mainly two different forms of the constitutive equations have been used for the viscoelastic stress tensor; namely Rivlin-Ericksen [8, 25, 26] and Criminale–Ericksen–Filbey (CEF) [3-5, 27] constitutive relations, both of which can be written respectively in direct notation as

$$\underline{\underline{\mathbf{T}}} = \mu \underline{\underline{\mathbf{A}}} + \alpha_1 \underline{\underline{\widehat{\mathbf{A}}}} + \alpha_2 \underline{\underline{\mathbf{A}}} \bullet \underline{\underline{\mathbf{A}}} \tag{2.2}$$

$$\underline{\underline{\mathbf{T}}} = \mu \underline{\underline{\mathbf{A}}} + 0.5\alpha_1 \underline{\underline{\widehat{\mathbf{A}}}} - \left(0.5\alpha_1 + \alpha_2\right) \underline{\underline{\mathbf{A}}} \bullet \underline{\underline{\mathbf{A}}} \tag{2.3}$$

These two forms of the constitutive equations for the stress tensor can be represented in the following general form as $\underline{\underline{\mathbf{T}}} = \underline{\underline{\boldsymbol{\tau}}} + \underline{\underline{\boldsymbol{\varepsilon}}}$ where $\underline{\underline{\boldsymbol{\tau}}} = \mu \underline{\underline{\mathbf{A}}}$ and $\underline{\underline{\boldsymbol{\varepsilon}}}$ represent in the given order the viscous and elastic components of the viscoelastic stress tensor. In some relevant literatures, the viscoelastic stress tensor $\underline{\underline{\mathbf{T}}}$ is also referred to as the extra stress tensor. Here, $\underline{\underline{\mathbf{A}}} = \nabla\vec{\mathbf{v}} + \left(\nabla\vec{\mathbf{v}}\right)^T$ and $\underline{\underline{\hat{\mathbf{A}}}} = \mathcal{D}\underline{\underline{\mathbf{A}}} / \mathcal{D}t$ are the deformation rate tensor and the kinematic tensor respectively where $\mathcal{D} / \mathcal{D}t$ is a convected time derivative operator, μ is the dynamic fluid viscosity, α_1 and α_2 are the first and the second normal stress difference coefficients. All of μ, α_1, and α_2 are material constants that can be determined by viscometric flows for any real fluid. The irreversible thermodynamic analysis on the second grade fluids performed by Dunn and Fosdick [25, 28] requires the satisfaction of the following restrictions $\mu > 0$, $\alpha_1 \geq 0$ and $\alpha_1 + \alpha_2 = 0$ so that all motions of the fluid are said to fulfill the Clausius–Duhem inequality. On the other hand, the experimental values of α_1 and α_2 for many non-Newtonian fluids which are assumed to obey the constitutive relation given in Equation (2.2) did not comply with the above given restriction; rather they satisfy the following conditions; $\mu > 0$, $\alpha_1 < 0$, and $\alpha_1 + \alpha_2 \neq 0$, which we have used in our simulations. The material parameters α_1 and α_2 are functions of the magnitude of the deformation rate tensor. In what follows, the following definitions apply; $N_1 = -\alpha_1 A_{xy}^2$, and $N_2 = -\alpha_2 A_{xy}^2$ where $N_1 = T_{xx} - T_{yy}$ and $N_2 = T_{yy} - T_{zz}$ are referred to as the first and second normal stress differences [5]. The second normal stress difference coefficient is difficult to measure, and also considerably smaller than the first normal stress difference coefficient; hence, in many earlier studies, it is either approximated through $\alpha_2 = -0.1 \text{ x } \alpha_1$, or neglected [3, 8, 27]. In the extrusion process, the second grade polymeric fluid can either swell or contract depending on the sign of first normal stress difference coefficient.

When the viscoelastic polymeric liquid is deformed under the action of either stretching or shearing, or the combination of these two processes, the polymer molecules get stretched and entangled. If the polymer melt is exposed to a deformation for a short period of time, polymer molecules do remember their initial configuration, thereby being able to recover their initial

shape. On the other hand, if the deformation is applied for an extended period of time, the polymer molecules tend to forget their initial positions, and in turn can not recover their original shape. This time dependent phenomenon is known as the viscoelastic memory effect or the stress relaxation effect. The viscoelastic memory of polymeric materials is scaled with a dimensionless number referred to as Deborah number, $De = \lambda / t$, which is defined as the ratio of the material relaxation time to the time scale of the flow (processing time). For die swell, the material relaxation time, defined as the time required for whole polymer molecules to relax and get used to its new state of deformation can be formulated as $\lambda = \alpha_1 / \mu$. The characteristic process time $t = h / \mathrm{v}$ can be approximated as the ratio of the characteristic die diameter to the average speed of the flow through the die so that Deborah number can be reformulated as $De = \alpha_1 \mathrm{v} / \mu h$. Note that the polymeric liquid behaves as a viscous fluid if Deborah number goes to zero, while it acts as an elastic solid if *De* goes to infinity.

2.4 Various Forms of Convected Time Derivatives

Our literature review on the die swell of a second-order fluid has showed that there are different forms of convected time derivatives as given in Table 2-1. Convected time derivative is an operator that transforms a tensor from convected to fixed coordinates. There are no clear guidelines that can be followed to determine which form of time derivative might be the best or most appropriate for predicting the rheological behaviour of polymeric fluids. Therefore, one should determine the usefulness of a given convected derivative based on its ability to predict the experimentally observed rheological behaviour of polymeric fluids. In the following, for the sake of completeness, we present those that we used in our simulation work to study their ability for predicting the die swell phenomenon correctly. The origin and the detailed derivations of these various forms of convected time derivatives can be found in [29].

Table 2-1: Various forms of convected time derivatives that transform a tensor from convected to fixed coordinates, given in both direct and component notations.

Convected derivatives	Formulation
Covariant form [25, 26]	$\mathcal{D}\underline{\underline{\mathbf{A}}}/\mathcal{D}t = D\underline{\underline{\mathbf{A}}}/Dt + (\nabla\vec{\mathbf{v}})\bullet\underline{\underline{\mathbf{A}}} + \underline{\underline{\mathbf{A}}}\bullet(\nabla\vec{\mathbf{v}})^T$ $\mathcal{D}A_{ij}/\mathcal{D}t = DA_{ij}/Dt + v_{k,i}A_{kj} + v_{k,j}A_{ik}$
Controvariant form [8, 9]	$\mathcal{D}\underline{\underline{\mathbf{A}}}/\mathcal{D}t = D\underline{\underline{\mathbf{A}}}/Dt - (\nabla\vec{\mathbf{v}})^T\bullet\underline{\underline{\mathbf{A}}} - \underline{\underline{\mathbf{A}}}\bullet(\nabla\vec{\mathbf{v}})$ $\mathcal{D}A_{ij}/\mathcal{D}t = DA_{ij}/Dt - v_{i,k}A_{kj} - v_{j,k}A_{ik}$
Mixed covariant-contravariant form [5]	$\mathcal{D}\underline{\underline{\mathbf{A}}}/\mathcal{D}t = D\underline{\underline{\mathbf{A}}}/Dt + (\nabla\vec{\mathbf{v}})^T\bullet\underline{\underline{\mathbf{A}}} - \underline{\underline{\mathbf{A}}}\bullet(\nabla\vec{\mathbf{v}})$ $\mathcal{D}A_{ij}/\mathcal{D}t = DA_{ij}/Dt + v_{i,k}A_{kj} - v_{j,k}A_{ik}$
Corotational (Jaumann) derivative [10]	$\mathcal{D}\underline{\underline{\mathbf{A}}}/\mathcal{D}t = D\underline{\underline{\mathbf{A}}}/Dt - \underline{\underline{\boldsymbol{\omega}}}\bullet\underline{\underline{\mathbf{A}}} - (\underline{\underline{\boldsymbol{\omega}}}\bullet\underline{\underline{\mathbf{A}}})^T$, where $\underline{\underline{\boldsymbol{\omega}}}$ is called the vorticity tensor, and defined as $\underline{\underline{\boldsymbol{\omega}}} = 0.5\left(\nabla\vec{\mathbf{v}} - (\nabla\vec{\mathbf{v}})^T\right)$, or in component form as $\omega_{ij} = 0.5(v_{i,j} - v_{j,i})$, $\mathcal{D}A_{ij}/\mathcal{D}t = DA_{ij}/Dt - \omega_{ik}A_{jk} - \omega_{jk}A_{ik}$

The physical interpretation of the right-hand side of covariant, contravariant, and mixed covariant and contravariant convected time derivatives can be given such that the first term on the right hand side represents the material time derivative of a tensor in the fixed coordinate systems, while the second and third terms represent the deformation (stretching) and rotational motions of a material element referred to in a fixed coordinate system as the velocity gradient tensor $v_{i,j}$ (and $v_{j,i}$) can be expressed by the sum of deformation rate tensor $d_{ij} = 0.5\ (v_{i,j} + v_{j,i})$ and the vorticity tensor $\omega_{ij} = 0.5\ (v_{i,j} - v_{j,i})$. Jaumann convected time derivative can be formed by adding covariant and contravariant convected time derivatives and then noting that $v_{i,j} = d_{ij} + \omega_{ij}$. The second and third terms on the right hand side of Jaumann derivative describe the rotational motion of the material element.

CHAPTER 3

3 SMOOTHED PARTICLE HYDRODYNAMICS

Smoothed particle hydrodynamics (SPH) is one of the members of meshless Lagrangian particle methods used to solve partial differential equations widely encountered in scientific and engineering problems. Unlike Eulerian (mesh-dependent) computational techniques such as finite difference, finite volume and finite element methods, SPH does not require a grid, as field derivatives are approximated analytically using a kernel function. In this technique, the continuum or the global computational domain is represented by a set of discrete particles instead of grids. Here, it should be noted that the term particle refers to a macroscopic part (geometrical position) in the continuum. Each particle carries mass, momentum, energy and other relevant hydrodynamic properties. These sets of particles are able to describe the physical behaviour of the continuum, also have the ability to move under the influence of the internal/external forces applied due to the Lagrangian nature of SPH [30, 31].

For clarity of the presentation, it is worthy of introducing notational conventions to be used throughout this work. All vector quantities are written either using the index notation with Latin indices denoting the components or direct notations with lowercase boldface letters. These components will be written either as subscripts (when particle identifiers are not used) or superscripts (when particle identifiers are used). As well, throughout this work the Einstein summation convention is employed, where any repeated component index is summed over the range of the index. These superscripts do not represent any covariant or contravariant nature. Latin boldface indices (**i**, **j**) will be used as particle identifiers to denote particles and will always be placed as subscripts that are not summed, unless indicated with a summation

symbol. For example, the position vector for particle **i** is $\vec{\mathrm{r}}_{\mathrm{i}} = x_{\mathrm{i}}^{k}\vec{\mathrm{e}}_{k}$ where $x_{\mathbf{i}}^{k}$ components of the position vector and $\vec{\mathbf{e}}_{k}$ is a base vector. The distance vector between a pair of particles is indicated by $\vec{\mathbf{r}}_{\mathbf{ij}} = \vec{\mathbf{r}}_{\mathbf{i}} - \vec{\mathbf{r}}_{\mathbf{j}} = \left(x_{\mathbf{i}}^{k} - x_{\mathbf{j}}^{k}\right)\vec{\mathbf{e}}_{k} = r_{\mathbf{ij}}^{k}\vec{\mathbf{e}}_{k}$, and the magnitude of the distance vector $\left\|\vec{\mathbf{r}}_{\mathbf{ij}}\right\|$ is denoted by $r_{\mathbf{ij}}$.

The three-dimensional Dirac-delta function $\delta^{3}\left(r_{\mathbf{ij}}\right)$, also referred to as a unit pulse function, is the starting point of the SPH approximation technique. This function satisfies the identity

$$f\left(\vec{\mathbf{r}}_{\mathbf{i}}\right) = \int_{\Omega} f\left(\vec{\mathbf{r}}_{\mathbf{j}}\right)\delta^{3}\left(r_{\mathbf{ij}}\right)d^{3}\vec{\mathbf{r}}_{\mathbf{j}} \tag{3.1}$$

where $d^{3}\vec{\mathbf{r}}_{\mathbf{j}}$ is a differential volume element and Ω represents the total bounded volume of the domain.

3.1 Kernel Function

The SPH approach assumes that fields of a given particle are affected by those of all other particles within the global domain. The interactions among the particles within the global domain are achieved through a compactly supported, normalized and even weighting function (smoothing kernel function) $W\left(r_{\mathbf{ij}}, h\right)$ with a smoothing radius κh (cut off distance, localized domain) beyond which the function is zero. Hence, in computations, a given particle interacts with only its nearest neighbors contained in this localized domain. Here, the length h defines the support domain of the particle of interest and κ is a coefficient associated with the particular kernel function, where $r_{\mathbf{ij}}$ is the magnitude of the distance between the particle of interest **i** and its neighbouring particles **j**. If the Dirac delta function in Equation (3.1) is replaced by a kernel function $W\left(r_{\mathbf{ij}}, h\right)$, the integral estimate or the kernel approximation to an arbitrary function $f\left(\vec{\mathbf{r}}_{\mathbf{i}}\right)$ can be introduced as

$$f\left(\vec{\mathbf{r}}_{\mathbf{i}}\right) \cong \left\langle f\left(\vec{\mathbf{r}}_{\mathbf{i}}\right)\right\rangle \equiv \int_{\Omega} f\left(\vec{\mathbf{r}}_{\mathbf{j}}\right) W\left(r_{\mathbf{ij}}, h\right) d^3\vec{\mathbf{r}}_{\mathbf{j}} \tag{3.2}$$

where the angle bracket $\langle\ \rangle$ denotes the kernel approximation, and $\vec{\mathbf{r}}_{\mathbf{i}}$ is the position vector defining the center point of the kernel function.

Approximation to the Dirac-delta function by a smoothing kernel function is the origin of the smoothed particle hydrodynamics. The Dirac-delta function can be replaced by a smoothing kernel function provided that the smoothing kernel satisfies the following several conditions [32]; namely, **(a)** *normalization condition:* the area under the smoothing function must be unity over its support domain, $\int_{\Omega} W\left(r_{\mathbf{ij}}, h\right) d^3\vec{\mathbf{r}}_{\mathbf{j}} = 1$, **(b)** *the Dirac-delta function* property: as the smoothing length approaches to zero, the Dirac-delta function should be recovered $\lim_{h\to 0} W\left(r_{\mathbf{ij}}, h\right) = \delta^3\left(r_{\mathbf{ij}}\right)$, **(c)** *compactness* or *compact support* which necessitates that the kernel function is zero beyond its compact support domain, $W\left(r_{\mathbf{ij}}, h\right) = 0$ when $r_{\mathbf{ij}} > \kappa h$, and **(d)** the kernel function is to be spherically symmetric even function, $W\left(r_{\mathbf{ij}}, h\right) = W\left(-r_{\mathbf{ij}}, h\right)$, **(e)** the smoothing function should be positive within the support domain, $W\left(r_{\mathbf{ij}}, h\right) > 0$ when $r_{\mathbf{ij}} < \kappa h$. Finally, the value of the smoothing function should decay with increasing distance away from the center particle. The smoothing function can be represented in a general form as $W\left(r_{\mathbf{ij}}, h\right) = \left(1/h^d\right) f\left(r_{\mathbf{ij}}/h\right)$ where d is the dimension of the problem, and f is a function. In literature, it is possible to find a wide variety of kernel functions which satisfy above-listed conditions, such as Gaussian, cubic or quintic kernel functions. The smoothing kernels can be considered as discretization schemes in mesh dependent techniques such as finite difference and volume. Stability, accuracy and the speed of SPH simulation heavily depend on the choice of the smoothing kernel distribution as well as the smoothing length.

In Equation (3.3) is given the piecewise cubic smoothing function

$$W\left(r_{ij},h_i\right)=a_{\dim}\begin{cases}\dfrac{2}{3}-s_{ij}^2+\dfrac{1}{2}s_{ij}^3 & \textbf{if } 0\le s_{ij}<1\\ \dfrac{1}{6}\left(2-s_{ij}\right)^3 & \textbf{if } 1\le s_{ij}<2\\ 0 & \textbf{if } s_{ij}\ge 2\end{cases} \tag{3.3}$$

where $s_{ij}=r_{ij}/h$, and $\alpha_{\dim}$ is a dimension dependent constant which takes the values of $\alpha_1=1/h$, $\alpha_2=15/7\pi h^2$, and $\alpha_3=3/2\pi h^3$ for one, two or three-dimensional space respectively. Our early experience showed that for fluid simulation at low Reynolds numbers (i.e., $\mathrm{Re}=1$), the cubic spline kernel produces inaccurate velocity fields and in turn inaccurate density fields, while the high-order quintic spline kernel is stable. Instability problem due to the usage of cubic spline shows itself clearly in 2-D cavity problem simulation. On the other hand, no instability problem was observed in the simulation of the one-dimensional Couette and Poiseuille flow at $\mathrm{Re}=1$. Therefore, throughout this work, we have used the compactly supported two-dimensional quintic spline kernel which is given in Equation (3.4) and Figure 3-1.

$$W\left(r_{ij},h\right)=\frac{7}{478\pi h^2}\begin{cases}\left(3-s_{ij}\right)^5-6\left(2-s_{ij}\right)^5+15\left(1-s_{ij}\right)^5 & \textbf{if } 0\le s_{ij}<1\\ \left(3-s_{ij}\right)^5-6\left(2-s_{ij}\right)^5 & \textbf{if } 1\le s_{ij}<2\\ \left(3-s_{ij}\right)^5 & \textbf{if } 2\le s_{ij}\le 3\\ 0 & \textbf{if } s_{ij}\ge 3\end{cases} \tag{3.4}$$

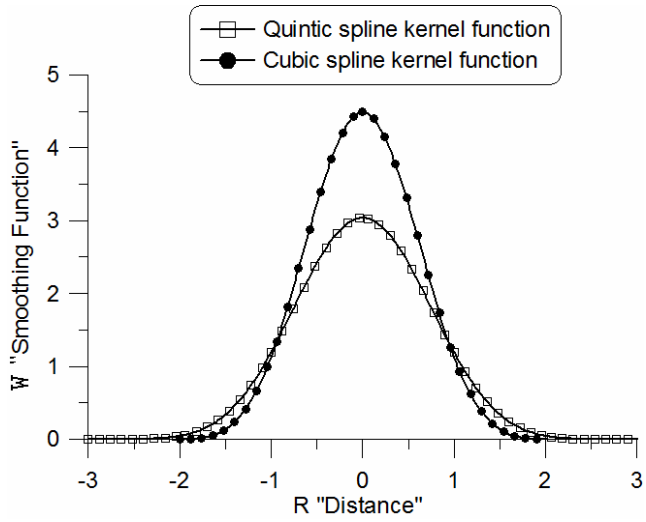

Figure 3-1: Quintic spline and cubic spline kernel function.

3.2 SPH Particle Interaction

The spatial resolution of SPH is affected by the smoothing length. Hence, depending on the problem to be solved, each particle can be assigned to a different value of smoothing length. However, for a variable smoothing length, it is probable to violate Newton's third law. For example, it might be possible for a particle **j** to exert a force on particle **i**, and not to experience an equal and opposite reaction force from particle **i**. To ensure that Newton's third law is not violated and the pair wise interaction among particles moving close to each other is achieved, the smoothing length is substituted by its average, defined as $h_{\mathbf{ij}} = 0.5\left(h_{\mathbf{i}} + h_{\mathbf{j}}\right)$. The averaged smoothing length ensures that particle **i** is within the influence domain of particle **j** and vice versa.

3.3 SPH Neighbor Search Algorithm

There are several known searching algorithms that will find and store neighboring particles. Recall that neighbour particles are those particles **j** that satisfy the condition $r_{\mathbf{ij}} \le \kappa h_{\mathbf{ij}}$ for a given particle **i**. The most direct approach for finding particle neighbours is to cycle through all particles, and check whether the above given condition is satisfied or not, storing the results. However, this algorithm searches all N particles for each of the N particles **i**. Therefore, this type of search procedure is of the order N×N in terms of computation searching effort required. A more efficient approach is the "box-sorting" algorithm, which is known to be of order N logN. This algorithm divides the domain into an ordered number of boxes, with side dimensions equal to $\kappa h_{\max}$ in length. Each of the N particles **i** is then catalogued by which box it is located in. Since the box side dimensions are chosen to be $\kappa h_{\max}$, a neighbor **j** of particle **i** must be located in one of the adjacent boxes to the box containing particle **i**. Therefore, instead of searching all N particles, one must search a much smaller group of

particles. Due to the much smaller computational expense, all simulations in this work used the box-sorting procedure.

3.4 Spatial Derivatives and Particle Approximation in SPH

The SPH approximation for the gradient of an arbitrary function (i.e., scalar, vectorial, or tensorial) can be written through the substitution $f\left(\vec{\mathbf{r}}_\mathbf{j}\right) \to \partial f\left(\vec{\mathbf{r}}_\mathbf{j}\right) / \partial x_\mathbf{j}^k$ in Equation (3.2) to produce

$$\frac{\partial f\left(\vec{\mathbf{r}}_\mathbf{i}\right)}{\partial x_\mathbf{i}^k} \cong \left\langle \frac{\partial f\left(\vec{\mathbf{r}}_\mathbf{i}\right)}{\partial x_\mathbf{i}^k} \right\rangle \equiv \int_\Omega \frac{\partial f\left(\vec{\mathbf{r}}_\mathbf{j}\right)}{\partial x_\mathbf{j}^k} W\left(r_{\mathbf{ij}}, h\right) d^3\vec{\mathbf{r}}_\mathbf{j} \tag{3.5}$$

Upon integrating the right hand side of Equation (3.5) by parts and then using the Green-Gauss theorem, one can write

$$\int_S f\left(\vec{\mathbf{r}}_\mathbf{j}\right) W\left(r_{\mathbf{ij}}, h\right) d^2\vec{\mathbf{r}}_\mathbf{j} - \int_\Omega f\left(\vec{\mathbf{r}}_\mathbf{j}\right) \frac{\partial W\left(r_{\mathbf{ij}}, h\right)}{\partial x_\mathbf{j}^k} d^3\vec{\mathbf{r}}_\mathbf{j} \tag{3.6}$$

The gradient of the kernel function referencing particle **i** and **j** can be written as

$$\frac{\partial W\left(r_{\mathbf{ij}}, h\right)}{\partial x_\mathbf{i}^k} = \frac{\partial W\left(r_{\mathbf{ij}}, h\right)}{\partial r_{\mathbf{ij}}} \frac{\partial r_{\mathbf{ij}}}{\partial x_\mathbf{i}^k} \text{ and } \frac{\partial W\left(r_{\mathbf{ij}}, h\right)}{\partial x_\mathbf{j}^k} = \frac{\partial W\left(r_{\mathbf{ij}}, h\right)}{\partial r_{\mathbf{ij}}} \frac{\partial r_{\mathbf{ij}}}{\partial x_\mathbf{j}^k} \tag{3.7}$$

$$\frac{\partial r_{\mathbf{ij}}}{\partial x_\mathbf{i}^k} = \frac{\partial \left(r_{\mathbf{ij}}^m r_{\mathbf{ij}}^m\right)^{1/2}}{\partial x_\mathbf{i}^k} = \frac{2 r_{\mathbf{ij}}^m \delta^{mk}}{2\left(r_{\mathbf{ij}}^m r_{\mathbf{ij}}^m\right)^{1/2}} = \frac{r_{\mathbf{ij}}^k}{r_{\mathbf{ij}}} \text{ and } \frac{\partial r_{\mathbf{ij}}}{\partial x_\mathbf{j}^k} = \frac{\partial \left(r_{\mathbf{ij}}^m r_{\mathbf{ij}}^m\right)^{1/2}}{\partial x_\mathbf{j}^k} = -\frac{2 r_{\mathbf{ij}}^m \delta^{mk}}{2\left(r_{\mathbf{ij}}^m r_{\mathbf{ij}}^m\right)^{1/2}} = -\frac{r_{\mathbf{ij}}^k}{r_{\mathbf{ij}}} \tag{3.8}$$

Combining Equations (3.7) and (3.8), one can show that

$$\partial W\left(r_{\mathbf{ij}}, h\right) / \partial x_\mathbf{i}^k = -\partial W\left(r_{\mathbf{ij}}, h\right) / \partial x_\mathbf{j}^k \tag{3.9}$$

Here, the first term in Equation (3.6) is referred to a boundary residual integral. Upon using compactness property of the kernel function which requires that the boundary residual integral is zero and Equation (3.9), it can be shown that

$$\frac{\partial f\left(\vec{\mathbf{r}}_{\mathbf{i}}\right)}{\partial x_{\mathbf{i}}^{k}} \cong \left\langle \frac{\partial f\left(\vec{\mathbf{r}}_{\mathbf{i}}\right)}{\partial x_{\mathbf{i}}^{k}} \right\rangle \equiv \int_{\Omega} f\left(\vec{\mathbf{r}}_{\mathbf{j}}\right) \frac{\partial W\left(r_{\mathbf{ij}}, h\right)}{\partial x_{\mathbf{i}}^{k}} d^{3}\vec{\mathbf{r}}_{\mathbf{j}} \tag{3.10}$$

The SPH approximation used for the gradient of a vector-valued function $f^{p}\left(\vec{\mathbf{r}}_{\mathbf{i}}\right)$ is an obvious extension of Equation (3.10) and is obtained by replacing $f\left(\vec{\mathbf{r}}_{\mathbf{i}}\right) \to f^{p}\left(\vec{\mathbf{r}}_{\mathbf{i}}\right)$.

In the following, we provide various forms of the SPH approximation of first-order derivative of a vector-valued function. The derivation is carried out in Cartesian coordinates. The SPH approximation for the gradient of a vectorial function starts with a Taylor series expansion of $f^{p}\left(\vec{\mathbf{r}}_{\mathbf{j}}\right)$ so that

$$f^{p}\left(\vec{\mathbf{r}}_{\mathbf{j}}\right) = f^{p}\left(\vec{\mathbf{r}}_{\mathbf{i}}\right) + r_{\mathbf{ji}}^{l} \frac{\partial f^{p}\left(\vec{\mathbf{r}}_{\mathbf{i}}\right)}{\partial x_{\mathbf{i}}^{l}}\Big|_{\vec{\mathbf{r}}_{\mathbf{j}}=\vec{\mathbf{r}}_{\mathbf{i}}} + \frac{1}{2} r_{\mathbf{ji}}^{l} r_{\mathbf{ji}}^{k} \frac{\partial f^{p}\left(\vec{\mathbf{r}}_{\mathbf{i}}\right)}{\partial x_{\mathbf{i}}^{l} \partial x_{\mathbf{i}}^{k}}\Big|_{\vec{\mathbf{r}}_{\mathbf{j}}=\vec{\mathbf{r}}_{\mathbf{i}}} + \mathsf{O}\left(h\right) \tag{3.11}$$

Upon multiplying Equation (3.11) by the term, $\partial W\left(r_{\mathbf{ij}}, h\right) / \partial x_{\mathbf{j}}^{s}$, and then integrating over the whole space $d^{3}\vec{\mathbf{r}}_{\mathbf{j}}$, one can write,

$$\begin{aligned} \int_{\Omega} \left(f^{p}\left(\vec{\mathbf{r}}_{\mathbf{j}}\right) - f^{p}\left(\vec{\mathbf{r}}_{\mathbf{i}}\right) \right) \frac{\partial W\left(r_{\mathbf{ij}}, h\right)}{\partial x_{\mathbf{j}}^{s}} d^{3}\vec{\mathbf{r}}_{\mathbf{j}} = \frac{\partial f^{p}\left(\vec{\mathbf{r}}_{\mathbf{i}}\right)}{\partial x_{\mathbf{i}}^{l}} \underbrace{\int_{\Omega} r_{\mathbf{ji}}^{l} \frac{\partial W\left(r_{\mathbf{ij}}, h\right)}{\partial x_{\mathbf{j}}^{s}} d^{3}\vec{\mathbf{r}}_{\mathbf{j}}}_{I^{ls}} \\ + \frac{1}{2} \frac{\partial f^{p}\left(\vec{\mathbf{r}}_{\mathbf{i}}\right)}{\partial x_{\mathbf{i}}^{l} \partial x_{\mathbf{i}}^{k}} \underbrace{\int_{\Omega} r_{\mathbf{ji}}^{l} r_{\mathbf{ji}}^{k} \frac{\partial W\left(r_{\mathbf{ij}}, h\right)}{\partial x_{\mathbf{j}}^{s}} d^{3}\vec{\mathbf{r}}_{\mathbf{j}}}_{I^{lks}=0} \end{aligned} \tag{3.12}$$

Note that the first and the second integrals on the right hand side of Equation (3.12) are, respectively, second- and third-rank tensors. The third-rank tensor I^{lks} can be integrated by parts, which upon using the Green-Gauss theorem produces Equation (3.13) since the kernel function $W\left(r_{\mathbf{ij}}, h\right)$ vanishes beyond its support domain.

$$I^{lks} = -\int_{\Omega} W\left(r_{\mathbf{ij}}, h\right) \frac{\partial}{\partial r_{\mathbf{j}}^{s}} \left(r_{\mathbf{ji}}^{l} r_{\mathbf{ji}}^{k}\right) d^{3}\vec{\mathbf{r}}_{\mathbf{j}} = -\int_{\Omega} W\left(r_{\mathbf{ij}}, h\right) \left(r_{\mathbf{ji}}^{l} \delta^{sk} + r_{\mathbf{ji}}^{k} \delta^{ls}\right) d^{3}\vec{\mathbf{r}}_{\mathbf{j}} \tag{3.13}$$

Recalling that the kernel function is spherically symmetric even function and the multiplication of an even function by an odd function produces an odd function. Integration of an odd function over a symmetric domain leads to zero.

$$I^{lks} = -\delta^{sk} \underbrace{\int_{\Omega} r_{\mathbf{ji}}^{l} W\left(r_{\mathbf{ij}}, h\right) d^{3}\vec{\mathbf{r}}_{\mathbf{j}}}_{=0} - \delta^{ls} \underbrace{\int_{\Omega} r_{\mathbf{ji}}^{k} W\left(r_{\mathbf{ij}}, h\right) d^{3}\vec{\mathbf{r}}_{\mathbf{j}}}_{=0} = 0 \tag{3.14}$$

Following the above described procedure identically, the second rank tensor can be written as

$$I^{ls} = -\delta^{ls} \underbrace{\int_{\Omega} W\left(r_{\mathbf{ij}}, h\right) d^{3}\vec{\mathbf{r}}_{\mathbf{ji}}}_{=1} = -\delta^{ls} \tag{3.15}$$

On combining Equation (3.12) with Equations (3.14) and (3.15), we can write,

$$\frac{\partial f^{p}\left(\vec{\mathbf{r}}_{\mathbf{i}}\right)}{\partial x_{\mathbf{i}}^{s}} = \int_{\Omega} \left(f^{p}\left(\vec{\mathbf{r}}_{\mathbf{j}}\right) - f^{p}\left(\vec{\mathbf{r}}_{\mathbf{i}}\right)\right) \frac{\partial W\left(r_{\mathbf{ij}}, h\right)}{\partial x_{\mathbf{i}}^{s}} d^{3}\vec{\mathbf{r}}_{\mathbf{j}} \tag{3.16}$$

Note that in Equation (3.16), the relationship $\partial W\left(r_{\mathbf{ij}}, h\right) / \partial x_{\mathbf{j}}^{s} = -\partial W\left(r_{\mathbf{ij}}, h\right) / \partial x_{\mathbf{i}}^{s}$ has been used. In the above equations, the SPH approximations are written for a continuous distribution. If, however, we recognize that these integrations will be carried out over all **N** discrete particles within the domain, the discrete SPH particle approximation can be obtained by replacing the integration with summation over particle **j** to produce the SPH approximation of a field property $f^{p}\left(\vec{\mathbf{r}}_{\mathbf{i}}\right)$ at particle **i** in terms of all other interacting particles **j**, and representing the particle volume as the ratio of a particle mass $m_{\mathbf{j}}$ and particle density $\rho_{\mathbf{j}}$.

Replacing the integration in Equation (3.16) with SPH summation over particle "**j**" and setting $d^{3}\vec{\mathbf{r}}_{\mathbf{j}} = m_{\mathbf{j}} / \rho_{\mathbf{j}}$, we can obtain the gradient of a vector-valued function in the form of SPH interpolation as.

$$\frac{\partial f^p\left(\vec{\mathbf{r}}_\mathbf{i}\right)}{\partial x_\mathbf{i}^s}=\sum_{\mathbf{j}=1}^{N}\frac{m_\mathbf{j}}{\rho_\mathbf{j}}\left(f^p\left(\vec{\mathbf{r}}_\mathbf{j}\right)-f^p\left(\vec{\mathbf{r}}_\mathbf{i}\right)\right)\frac{\partial W\left(r_{\mathbf{ij}},h\right)}{\partial x_\mathbf{i}^s} \tag{3.17}$$

There are other alternative forms for the SPH gradient approximation of an arbitrary function. One that is also used within the context of this presentation can be formulated through using the product rule of differentiation on $\partial\left(f^k\left(\vec{\mathbf{r}}_\mathbf{i}\right)/\rho_\mathbf{i}\right)/\partial x_\mathbf{i}^s$ in combination with Equation (3.10). In what follows, one can write,

$$\frac{1}{\rho_\mathbf{i}}\frac{\partial f^k\left(\vec{\mathbf{r}}_\mathbf{i}\right)}{\partial x_\mathbf{i}^s}=\sum_{\mathbf{j}=1}^{N}m_\mathbf{j}\left(\frac{f^k\left(\vec{\mathbf{r}}_\mathbf{i}\right)}{\rho_\mathbf{i}^2}+\frac{f^k\left(\vec{\mathbf{r}}_\mathbf{j}\right)}{\rho_\mathbf{j}^2}\right)\frac{\partial W\left(r_{\mathbf{ij}},h\right)}{\partial x_\mathbf{i}^s} \tag{3.18}$$

Here, we present an approximation to the second order spatial derivative of a vector-valued function. Consider a well-behaved (continuous) vector-valued function $f^p\left(\vec{\mathbf{r}}\right)$ of the position vector $\vec{\mathbf{r}}$. Since SPH approximates the continuum with the ensemble of discrete points (particles), these function will take different values at each particle, which will be indicated by notation $f^p\left(\vec{\mathbf{r}}_\mathbf{i}\right)$ and $f^p\left(\vec{\mathbf{r}}_\mathbf{j}\right)$. Here, $f^p\left(\vec{\mathbf{r}}_\mathbf{i}\right)$ denotes the value of the field at particle $\vec{\mathbf{r}}_\mathbf{i}$ (particle of interest for which field is to be computed), while $f^p\left(\vec{\mathbf{r}}_\mathbf{j}\right)$ indicates the field value possessed by neighbor particles. In other words, both $f^p\left(\vec{\mathbf{r}}_\mathbf{i}\right)$ and $f^p\left(\vec{\mathbf{r}}_\mathbf{j}\right)$ are functions of the position vector $\vec{\mathbf{r}}$, but they reference different particles. For the function $f^p\left(\vec{\mathbf{r}}\right)$, we can approximate $f^p\left(\vec{\mathbf{r}}_\mathbf{j}\right)$ by Taylor expansion in the proximity of $f\left(\vec{\mathbf{r}}_\mathbf{i}\right)$ as,

$$f^p\left(\vec{\mathbf{r}}_\mathbf{j}\right)=f^p\left(\vec{\mathbf{r}}_\mathbf{i}\right)+r_{\mathbf{ji}}^l\frac{\partial f^p\left(\vec{\mathbf{r}}_\mathbf{i}\right)}{\partial x_\mathbf{i}^l}+\frac{1}{2}r_{\mathbf{ji}}^l r_{\mathbf{ji}}^k\frac{\partial f^p\left(\vec{\mathbf{r}}_\mathbf{i}\right)}{\partial x_\mathbf{i}^l\partial x_\mathbf{i}^k}+\mathsf{O}\left(h\right) \tag{3.19}$$

On multiplying the Taylor expansion in Equation (3.19) by $\frac{r_{\mathbf{ij}}^s}{r_{\mathbf{ij}}{}^2}\frac{\partial W\left(r_{\mathbf{ij}},h\right)}{\partial x_\mathbf{i}^m}$, and then integrating over the whole space $d^3\vec{\mathbf{r}}_\mathbf{j}$, one can write,

$$\int_{\Omega}\left(f^{p}\left(\vec{\mathbf{r}}_{\mathbf{j}}\right)-f^{p}\left(\vec{\mathbf{r}}_{\mathbf{i}}\right)\right)\frac{r_{\mathbf{ij}}^{s}}{r_{\mathbf{ij}}^{2}}\frac{\partial W\left(r_{\mathbf{ij}},h\right)}{\partial x_{\mathbf{i}}^{m}}d^{3}\vec{\mathbf{r}}_{\mathbf{j}}=\frac{\partial f^{p}\left(\vec{\mathbf{r}}_{\mathbf{i}}\right)}{\partial x_{\mathbf{i}}^{l}}\int_{\Omega}\frac{r_{\mathbf{ji}}^{l}r_{\mathbf{ji}}^{s}}{r_{\mathbf{ij}}^{2}}\frac{\partial W\left(r_{\mathbf{ij}},h\right)}{\partial x_{\mathbf{j}}^{m}}d^{3}\vec{\mathbf{r}}_{\mathbf{j}}+\frac{1}{2}\frac{\partial^{2}f^{p}\left(\vec{\mathbf{r}}_{\mathbf{i}}\right)}{\partial x_{\mathbf{i}}^{l}\partial x_{\mathbf{i}}^{k}}\int_{\Omega}\frac{r_{\mathbf{ji}}^{l}r_{\mathbf{ji}}^{k}r_{\mathbf{ji}}^{s}}{r_{\mathbf{ij}}^{2}}\frac{\partial W\left(r_{\mathbf{ij}},h\right)}{\partial x_{\mathbf{j}}^{m}}d^{3}\vec{\mathbf{r}}_{\mathbf{j}} \tag{3.20}$$

where the relationship $\partial W\left(r_{\mathbf{ij}},h\right)/\partial x_{\mathbf{j}}^{m}=-\partial W\left(r_{\mathbf{ij}},h\right)/\partial x_{\mathbf{i}}^{m}$ has been used.

The first integral on the right-side of Equation (3.20) is a third rank tensor that vanishes due to spherical symmetry and isotropy. Therefore, Equation (3.20) reduces to

$$2\int_{\Omega}\left(f^{p}\left(\vec{\mathbf{r}}_{\mathbf{i}}\right)-f^{p}\left(\vec{\mathbf{r}}_{\mathbf{j}}\right)\right)\frac{r_{\mathbf{ij}}^{s}}{r_{\mathbf{ij}}^{2}}\frac{\partial W\left(r_{\mathbf{ij}},h\right)}{\partial x_{\mathbf{i}}^{m}}d^{3}\vec{\mathbf{r}}_{\mathbf{j}}=-\frac{\partial^{2}f^{p}\left(\vec{\mathbf{r}}_{\mathbf{i}}\right)}{\partial x_{\mathbf{i}}^{l}\partial x_{\mathbf{i}}^{k}}\int_{\Omega}r_{\mathbf{ji}}^{s}\underbrace{\frac{r_{\mathbf{ji}}^{l}r_{\mathbf{ji}}^{k}}{r_{\mathbf{ij}}^{2}}}_{\hat{r}_{\mathbf{ji}}^{l}\hat{r}_{\mathbf{ji}}^{k}}\frac{\partial W\left(r_{\mathbf{ij}},h\right)}{\partial x_{\mathbf{j}}^{m}}d^{3}\vec{\mathbf{r}}_{\mathbf{j}} \tag{3.21}$$

The integral on the right hand side of Equation (3.21) is a fourth-rank tensor and can be written in the following form by using integration by part as

$$\int_{\Omega}\hat{r}_{\mathbf{ji}}^{l}\hat{r}_{\mathbf{ji}}^{k}r_{\mathbf{ji}}^{s}\frac{\partial W\left(r_{\mathbf{ij}},h\right)}{\partial x_{\mathbf{j}}^{m}}d^{3}\vec{\mathbf{r}}_{\mathbf{j}}=\int_{\Omega}\frac{\partial}{\partial x_{\mathbf{j}}^{m}}\left(\hat{r}_{\mathbf{ji}}^{l}\hat{r}_{\mathbf{ji}}^{k}r_{\mathbf{ji}}^{s}W\left(r_{\mathbf{ij}},h\right)\right)d^{3}\vec{\mathbf{r}}_{\mathbf{j}}-\int_{\Omega}W\left(r_{\mathbf{ij}},h\right)\frac{\partial}{\partial x_{\mathbf{j}}^{m}}\left(\hat{r}_{\mathbf{ji}}^{l}\hat{r}_{\mathbf{ji}}^{k}r_{\mathbf{ji}}^{s}\right)d^{3}\vec{\mathbf{r}}_{\mathbf{j}} \tag{3.22}$$

Upon applying the Green-Gauss theorem on the first integral on the right hand side of Equation (3.22), we can write,

$$\int_{\Omega}\frac{\partial}{\partial x_{\mathbf{j}}^{m}}\left(\hat{r}_{\mathbf{ji}}^{l}\hat{r}_{\mathbf{ji}}^{k}r_{\mathbf{ji}}^{s}W\left(r_{\mathbf{ij}},h\right)\right)d^{3}\vec{\mathbf{r}}_{\mathbf{j}}=\int_{S}\hat{r}_{\mathbf{ji}}^{l}\hat{r}_{\mathbf{ji}}^{k}r_{\mathbf{ji}}^{s}W\left(r_{\mathbf{ij}},h\right)d^{2}\vec{\mathbf{r}}_{\mathbf{j}}=0 \tag{3.23}$$

where we have a vanishing surface integral for all the interior particles since the kernel goes to zero at the boundaries. Therefore, Equation (3.22) reduces to,

$$\int_{\Omega}\hat{r}_{\mathbf{ji}}^{l}\hat{r}_{\mathbf{ji}}^{k}r_{\mathbf{ji}}^{s}\frac{\partial W\left(r_{\mathbf{ij}},h\right)}{\partial x_{\mathbf{j}}^{m}}d^{3}\vec{\mathbf{r}}_{\mathbf{j}}=-\int_{\Omega}W\left(r_{\mathbf{ij}},h\right)\frac{\partial}{\partial x_{\mathbf{j}}^{m}}\left(\hat{r}_{\mathbf{ji}}^{l}\hat{r}_{\mathbf{ji}}^{k}r_{\mathbf{ji}}^{s}\right)d^{3}\vec{\mathbf{r}}_{\mathbf{j}} \tag{3.24}$$

In the following is presented some mathematical manipulations required for the evaluation of the partial derivative on the right hand side of Equation (3.24).

$$\frac{\partial r_{\mathbf{ij}}}{\partial x_{\mathbf{j}}^m}=\frac{\partial\left(r_{\mathbf{ji}}^p r_{\mathbf{ji}}^p\right)^{1/2}}{\partial x_{\mathbf{j}}^m}=\frac{\left(r_{\mathbf{ji}}^p r_{\mathbf{ji}}^p\right)^{-1/2}}{2}\left(r_{\mathbf{ji}}^p\underbrace{\frac{\partial r_{\mathbf{ji}}^p}{\partial x_{\mathbf{j}}^m}}_{\delta^{mp}}+r_{\mathbf{ji}}^p\underbrace{\frac{\partial r_{\mathbf{ji}}^p}{\partial x_{\mathbf{j}}^m}}_{\delta^{mp}}\right)=\frac{r_{\mathbf{ji}}^m}{r_{\mathbf{ij}}}$$

$$\frac{\partial \hat{r}_{\mathbf{ji}}^l}{\partial x_{\mathbf{j}}^m}=\frac{\partial}{\partial x_{\mathbf{j}}^m}\left(r_{\mathbf{ji}}^l/r_{\mathbf{ij}}\right)=\frac{1}{r_{\mathbf{ij}}^2}\left(r_{\mathbf{ij}}\underbrace{\frac{\partial r_{\mathbf{ji}}^l}{\partial x_{\mathbf{j}}^m}}_{=\delta^{lm}}-r_{\mathbf{ji}}^l\underbrace{\frac{\partial r_{\mathbf{ij}}}{\partial x_{\mathbf{j}}^m}}_{=r_{\mathbf{ji}}^m/r_{\mathbf{ij}}}\right)=\frac{1}{r_{\mathbf{ij}}}\left(\delta^{lm}-\hat{r}_{\mathbf{ji}}^l\hat{r}_{\mathbf{ji}}^m\right) \tag{3.25}$$

$$\frac{\partial}{\partial x_{\mathbf{j}}^m}\left(\hat{r}_{\mathbf{ji}}^l\hat{r}_{\mathbf{ji}}^k r_{\mathbf{ji}}^s\right)=\hat{r}_{\mathbf{ji}}^k\hat{r}_{\mathbf{ji}}^s\left(\delta^{lm}-\hat{r}_{\mathbf{ji}}^l\hat{r}_{\mathbf{ji}}^m\right)+\hat{r}_{\mathbf{ji}}^l\hat{r}_{\mathbf{ji}}^s\left(\delta^{km}-\hat{r}_{\mathbf{ji}}^k\hat{r}_{\mathbf{ji}}^m\right)+\delta^{sm}\hat{r}_{\mathbf{ji}}^l\hat{r}_{\mathbf{ji}}^k$$

$$\frac{\partial}{\partial x_{\mathbf{j}}^m}\left(\hat{r}_{\mathbf{ji}}^l\hat{r}_{\mathbf{ji}}^k r_{\mathbf{ji}}^s\right)=\hat{r}_{\mathbf{ji}}^l\hat{r}_{\mathbf{ji}}^s\delta^{km}-2\hat{r}_{\mathbf{ji}}^s\hat{r}_{\mathbf{ji}}^m\hat{r}_{\mathbf{ji}}^k\hat{r}_{\mathbf{ji}}^l+\hat{r}_{\mathbf{ji}}^k\hat{r}_{\mathbf{ji}}^s\delta^{lm}+\delta^{sm}\hat{r}_{\mathbf{ji}}^l\hat{r}_{\mathbf{ji}}^k$$

Casting Equations (3.24) and (3.25) into Equation (3.21), we can write

$$2\int_{\Omega}\left(f^p\left(\vec{\mathbf{r}}_{\mathbf{i}}\right)-f^p\left(\vec{\mathbf{r}}_{\mathbf{j}}\right)\right)\frac{r_{\mathbf{ij}}^s}{r_{\mathbf{ij}}^2}\frac{\partial W\left(r_{\mathbf{ij}},h\right)}{\partial x_{\mathbf{i}}^m}d^3\vec{\mathbf{r}}_{\mathbf{j}}=$$
$$\frac{\partial^2 f^p\left(\vec{\mathbf{r}}_{\mathbf{i}}\right)}{\partial x_{\mathbf{i}}^l\partial x_{\mathbf{i}}^k}\left(\begin{array}{l}\int_{\Omega}W\left(r_{\mathbf{ij}},h\right)\hat{r}_{\mathbf{ji}}^l\hat{r}_{\mathbf{ji}}^s\delta^{km}d^3\vec{\mathbf{r}}_{\mathbf{j}}-2\int_{\Omega}W\left(r_{\mathbf{ij}},h\right)\hat{r}_{\mathbf{ji}}^s\hat{r}_{\mathbf{ji}}^m\hat{r}_{\mathbf{ji}}^k\hat{r}_{\mathbf{ji}}^l d^3\vec{\mathbf{r}}_{\mathbf{j}}\\+\int_{\Omega}W\left(r_{\mathbf{ij}},h\right)\hat{r}_{\mathbf{ji}}^k\hat{r}_{\mathbf{ji}}^s\delta^{lm}d^3\vec{\mathbf{r}}_{\mathbf{j}}+\int_{\Omega}W\left(r_{\mathbf{ij}},h\right)\delta^{sm}\hat{r}_{\mathbf{ji}}^l\hat{r}_{\mathbf{ji}}^k d^3\vec{\mathbf{r}}_{\mathbf{j}}\end{array}\right) \tag{3.26}$$

Upon contracting on indices *m* and *s* in Equation (3.26), one can obtain

$$2\int_{\Omega}\left(f^p\left(\vec{\mathbf{r}}_{\mathbf{i}}\right)-f^p\left(\vec{\mathbf{r}}_{\mathbf{j}}\right)\right)\frac{r_{\mathbf{ij}}^s}{r_{\mathbf{ij}}^2}\frac{\partial W\left(r_{\mathbf{ij}},h\right)}{\partial x_{\mathbf{i}}^s}d^3\vec{\mathbf{r}}_{\mathbf{j}}=\frac{\partial^2 f^p\left(\vec{\mathbf{r}}_{\mathbf{i}}\right)}{\partial x_{\mathbf{i}}^l\partial x_{\mathbf{i}}^k}\int_{\Omega}W\left(r_{\mathbf{ij}},h\right)3\hat{r}_{\mathbf{ji}}^l\hat{r}_{\mathbf{ji}}^k d^3\vec{\mathbf{r}}_{\mathbf{j}} \tag{3.27}$$

The integral on the right hand side of Equation (3.27) is a second rank isotropic tensor since the spherically symmetric kernel function is multiplied by an even function. Recalling that Kronecker delta δ^{kl} are components of an isotropic tensor, an isotropic tensor might be expressed in terms of the Kronecker delta multiplied with a constant "c". Therefore, one can write

$$\int_{\Omega}W\left(r_{\mathbf{ij}},h\right)\hat{r}_{\mathbf{ji}}^l\hat{r}_{\mathbf{ji}}^k d^3\vec{\mathbf{r}}_{\mathbf{j}}=c\delta^{kl} \tag{3.28}$$

Taking the trace of Equation (3.28), we can show that c=1/3 where we have used the fact that $\hat{r}_{\mathbf{ji}}^{l}\hat{r}_{\mathbf{ji}}^{l}=1$ and $\int_{\Omega}W\left(r_{\mathbf{ij}},h\right)d^{3}\vec{\mathbf{r}}_{\mathbf{j}}=1$ since the kernel used is properly normalized even function. Substituting Equation (3.28) into Equation (3.27), one can obtain an approximation to a Laplacian of a vector-valued function as

$$\frac{\partial^{2}f^{p}\left(\vec{\mathbf{r}}_{\mathbf{i}}\right)}{\partial x_{\mathbf{i}}^{k}\partial x_{\mathbf{i}}^{k}}=2\int_{\Omega}\left(f^{p}\left(\vec{\mathbf{r}}_{\mathbf{i}}\right)-f^{p}\left(\vec{\mathbf{r}}_{\mathbf{j}}\right)\right)\frac{r_{\mathbf{ij}}^{s}}{r_{\mathbf{ij}}{}^{2}}\frac{\partial W\left(r_{\mathbf{ij}},h\right)}{\partial x_{\mathbf{i}}^{s}}d^{3}\vec{\mathbf{r}}_{\mathbf{j}} \tag{3.29}$$

To be able to derive an equation for the SPH approximation to the second order spatial derivative of the vector-valued function, we start with Equation (3.26). The second and fourth-rank tensors on the right hand side of Equation (3.26) are isotropic tensors due to the spherically symmetric kernel. It is easy to verify that the fourth-rank tensors with components of $\delta^{sm}\delta^{kl}$, $\delta^{sk}\delta^{ml}$ and $\delta^{sl}\delta^{mk}$ are also isotropic. Consequently, it follows that

$$a^{smkl}=c_{1}\delta^{sm}\delta^{kl}+c_{2}\delta^{sk}\delta^{ml}+c_{3}\delta^{sl}\delta^{mk} \tag{3.30}$$

where c_1, c_2 and c_3 are scalar coefficients and a^{smkl} are the components of a fourth rank tensor. Since the fourth rank tensor in Equation (3.26) is symmetric for all indices, it is easy to show that all the coefficients have to be equal to each other, namely $c_1=c_2=c_3$. In what follows, one can write the isotropic second and fourth rank tensors in Equation (3.26) as

$$\begin{aligned}
&\int_{\Omega}W\left(r_{\mathbf{ij}},h\right)\hat{r}_{\mathbf{ji}}^{l}\hat{r}_{\mathbf{ji}}^{s}\delta^{km}d^{3}\vec{\mathbf{r}}_{\mathbf{j}}=\frac{\delta^{km}\delta^{ls}}{3}\\
&\int_{\Omega}W\left(r_{\mathbf{ij}},h\right)\hat{r}_{\mathbf{ji}}^{k}\hat{r}_{\mathbf{ji}}^{s}\delta^{lm}d^{3}\vec{\mathbf{r}}_{\mathbf{j}}=\frac{\delta^{lm}\delta^{ks}}{3}\\
&\int_{\Omega}W\left(r_{\mathbf{ij}},h\right)\delta^{sm}\hat{r}_{\mathbf{ji}}^{l}\hat{r}_{\mathbf{ji}}^{k}d^{3}\vec{\mathbf{r}}_{\mathbf{j}}=\frac{\delta^{sm}\delta^{kl}}{3}\\
&-2\int_{\Omega}W\left(r_{\mathbf{ij}},h\right)\hat{r}_{\mathbf{ji}}^{s}\hat{r}_{\mathbf{ji}}^{m}\hat{r}_{\mathbf{ji}}^{k}\hat{r}_{\mathbf{ji}}^{l}d^{3}\vec{\mathbf{r}}_{\mathbf{j}}=-2c_{1}\left(\delta^{sm}\delta^{kl}+\delta^{sk}\delta^{ml}+\delta^{sl}\delta^{mk}\right)
\end{aligned} \tag{3.31}$$

Equation (3.31) can be arranged in the flowing form

$$\left(\begin{array}{l}\int_{\Omega} W\left(r_{\mathbf{ij}},h\right)\hat{r}_{\mathbf{ji}}^{l}\hat{r}_{\mathbf{ji}}^{s}\delta^{km}d^{3}\vec{\mathbf{r}}_{\mathbf{j}}-2\int_{\Omega} W\left(r_{\mathbf{ij}},h\right)\hat{r}_{\mathbf{ji}}^{s}\hat{r}_{\mathbf{ji}}^{m}\hat{r}_{\mathbf{ji}}^{k}\hat{r}_{\mathbf{ji}}^{l}d^{3}\vec{\mathbf{r}}_{\mathbf{j}} \\ +\int_{\Omega} W\left(r_{\mathbf{ij}},h\right)\hat{r}_{\mathbf{ji}}^{k}\hat{r}_{\mathbf{ji}}^{s}\delta^{lm}d^{3}\vec{\mathbf{r}}_{\mathbf{j}}+\int_{\Omega} W\left(r_{\mathbf{ij}},h\right)\delta^{sm}\hat{r}_{\mathbf{ji}}^{l}\hat{r}_{\mathbf{ji}}^{k}d^{3}\vec{\mathbf{r}}_{\mathbf{j}}\end{array}\right)=\left(\frac{1}{3}-2c_{1}\right)\left(\delta^{sm}\delta^{kl}+\delta^{ls}\delta^{km}+\delta^{sk}\delta^{ml}\right) \tag{3.32}$$

Substituting Equation (3.32) into Equation (3.26), we can write

$$2\int_{\Omega}\left(f^{p}\left(\vec{\mathbf{r}}_{\mathbf{i}}\right)-f^{p}\left(\vec{\mathbf{r}}_{\mathbf{j}}\right)\right)\frac{r_{\mathbf{ij}}^{s}}{r_{\mathbf{ij}}^{2}}\frac{\partial W\left(r_{\mathbf{ij}},h\right)}{\partial x_{\mathbf{i}}^{m}}d^{3}\vec{\mathbf{r}}_{\mathbf{j}}=\frac{\partial^{2}f^{p}\left(\vec{\mathbf{r}}_{\mathbf{i}}\right)}{\partial x_{\mathbf{i}}^{s}\partial x_{\mathbf{i}}^{m}}\left(\frac{2}{3}-4c_{1}\right)+\left(\frac{1}{3}-2c_{1}\right)\frac{\partial^{2}f^{p}\left(\vec{\mathbf{r}}_{\mathbf{i}}\right)}{\partial x_{\mathbf{i}}^{k}\partial x_{\mathbf{i}}^{k}}\delta^{sm} \tag{3.33}$$

Upon contracting on indices *m* and *s* in Equation (3.33), one can obtain the value of coefficient c_1 as 1/24 and 1/15 for two and three dimensions, respectively. In what follows, Equation (3.33) is written in three dimensions as

$$2\int_{\Omega}\left(f^{p}\left(\vec{\mathbf{r}}_{\mathbf{i}}\right)-f^{p}\left(\vec{\mathbf{r}}_{\mathbf{j}}\right)\right)\frac{r_{\mathbf{ij}}^{s}}{r_{\mathbf{ij}}^{2}}\frac{\partial W\left(r_{\mathbf{ij}},h\right)}{\partial x_{\mathbf{i}}^{m}}d^{3}\vec{\mathbf{r}}_{\mathbf{j}}=\frac{2}{4}\frac{\partial^{2}f^{p}\left(\vec{\mathbf{r}}_{\mathbf{i}}\right)}{\partial x_{\mathbf{i}}^{s}\partial x_{\mathbf{i}}^{m}}+\frac{1}{4}\frac{\partial^{2}f^{p}\left(\vec{\mathbf{r}}_{\mathbf{i}}\right)}{\partial x_{\mathbf{i}}^{k}\partial x_{\mathbf{i}}^{k}}\delta^{sm} \tag{3.34}$$

Combining Equations (3.29) and (3.34) together with the relation $\frac{\partial W\left(r_{\mathbf{ij}},h\right)}{\partial x_{\mathbf{i}}^{m}}=\frac{r_{\mathbf{ij}}^{m}}{r_{\mathbf{ij}}}\frac{\partial W\left(r_{\mathbf{ij}},h\right)}{\partial r_{\mathbf{ij}}}$, one can write,

$$\frac{\partial^{2}f^{p}\left(\vec{\mathbf{r}}_{\mathbf{i}}\right)}{\partial x_{\mathbf{i}}^{s}\partial x_{\mathbf{i}}^{m}}=\int_{\Omega}\left(f^{p}\left(\vec{\mathbf{r}}_{\mathbf{i}}\right)-f^{p}\left(\vec{\mathbf{r}}_{\mathbf{j}}\right)\right)\frac{1}{r_{\mathbf{ij}}}\left(\frac{4r_{\mathbf{ij}}^{s}r_{\mathbf{ij}}^{m}}{r_{\mathbf{ij}}^{2}}-\delta^{sm}\right)\frac{\partial W\left(r_{\mathbf{ij}},h\right)}{\partial r_{\mathbf{ij}}}d^{3}\vec{\mathbf{r}}_{\mathbf{j}} \tag{3.35}$$

The discrete SPH particle approximation for the second-order derivative of a vector-valued function $\partial^{2}f^{p}\left(\vec{\mathbf{r}}_{\mathbf{i}}\right)/\partial x_{\mathbf{i}}^{s}\partial x_{\mathbf{i}}^{m}$ can be written [33] as

$$\frac{\partial^{2}f^{p}\left(\vec{\mathbf{r}}_{\mathbf{i}}\right)}{\partial x_{\mathbf{i}}^{s}\partial x_{\mathbf{i}}^{m}}=\sum_{\mathbf{j}=1}^{N}\frac{m_{\mathbf{j}}}{\rho_{\mathbf{j}}}\left(f^{p}\left(\vec{\mathbf{r}}_{\mathbf{i}}\right)-f^{p}\left(\vec{\mathbf{r}}_{\mathbf{j}}\right)\right)\frac{1}{r_{\mathbf{ij}}}\left(\frac{4r_{\mathbf{ij}}^{s}r_{\mathbf{ij}}^{m}}{r_{\mathbf{ij}}^{2}}-\delta^{kl}\right)\frac{\partial W\left(r_{\mathbf{ij}},h\right)}{\partial r_{\mathbf{ij}}} \tag{3.36}$$

The approximation for the Laplacian comes by contracting on indices *s* and *m* in Equation (3.36) to produce

$$\frac{\partial^2 f^p(\vec{\mathbf{r}}_\mathbf{i})}{\partial x_\mathbf{i}^k \partial x_\mathbf{i}^k} = 2\sum_{\mathbf{j}=1}^{N} \frac{m_\mathbf{j}}{\rho_\mathbf{j}} \left(f^p(\vec{\mathbf{r}}_\mathbf{i}) - f^p(\vec{\mathbf{r}}_\mathbf{j}) \right) \frac{1}{r_{\mathbf{ij}}} \frac{\partial W(r_{\mathbf{ij}}, h)}{\partial r_{\mathbf{ij}}} \tag{3.37}$$

3.5 SPH Solution Algorithms

There are two common approaches utilized in the SPH literature for solving the balance of the linear momentum equation. The first one is widely referred to as the weakly compressible SPH (WSPH) where the pressure term in the momentum equation is determined through an artificial equation of state. In the second approach which is known as incompressible SPH (ISPH), the pressure is computed by means of solving a pressure Poisson equation. In this work, we have implemented both WSPH and ISPH approaches. The artificial equation of state used in the WSPH approach has the form of, $p - p_o = c_\mathbf{i}^2 (\rho - \rho_o)$, where ρ_o, p_o and c are the reference density (taken as the real fluid density), reference pressure, and the speed of sound. This state equation enforces the incompressibility condition on the flow such that a small variation in density produces a relatively large change in pressure whereby preventing the dilatation of the fluid. The speed of sound $c_\mathbf{i}$ for each particle must be chosen carefully to ensure that the fluid is very closely incompressible. It has been suggested by Morris et.al. [21] that the square of the sound speed be chosen such that

$$c_\mathbf{i}^2 \approx \varphi \; max\left(\frac{v_{\max}^2}{\delta}, \frac{\mu}{\rho_o}\left(\frac{v_{\max}}{L_o \delta} \right), \frac{F^B L_o}{\delta} \right) \tag{3.38}$$

where φ is problem dependent coefficient, $v_{\max}$ is the maximum value of the fluid velocity, L_o is a characteristic length, F^B is a body force, δ is the relative incompressibility or the density variation factor, which is defined as $\delta = \Delta\rho / \rho_o = v_{\max}^2 / c_\mathbf{i}^2 = M^2$, where M is the Mach number. Upon selecting the sound speed much larger than the fluid velocity (at least an order of magnitude) thereby resulting in a very small Mach number, the density variation can be limited to 1% ($\delta \approx 0.01$), which is used in this work. Our own experience as well as recent reports in the literature has indicated that the rules of thumb given by Equation (3.38) are not

adequate for some problems. In this case, the problem dependent coefficient can be used to impose incompressibility condition for the simulated flow problems. In this presentation, we set $\varphi \approx 4$. The speed of sound chosen has a direct effect on the permissible time-step in a given simulation. The algorithm stability is controlled by the Courant-Friedrichs-Lewy (CFL) condition, where the recommended time-step [34] is $\Delta t \le C_{CFL} h_{\mathbf{ij},\min} / \left(c_{\mathbf{i}} + v_{\max}\right)$ where $h_{\mathbf{ij}} = 0.5\left(h_{\mathbf{i}} + h_{\mathbf{j}}\right)$, $h_{\mathbf{ij},min}$ is the minimum smoothing length among all **i-j** particle pairs, C_{CFL} is a constant satisfying $0 < C_{CFL} \le 1$ (in this work, $C_{CFL} = 0.125$)

In order to increment the time-steps in WSPH algorithm, we have used a leapfrog predictor corrector method. This technique is an explicit time integration scheme, and is relatively simple to implement. Particle positions, densities, and velocities are computed respectively as

$$D\vec{\mathbf{r}}_{\mathbf{i}} / Dt = \vec{\mathbf{v}}_{\mathbf{i}},\ D\rho_{\mathbf{i}} / Dt = k_{\mathbf{i}},\ D\vec{\mathbf{v}}_{\mathbf{i}} / Dt = \vec{\mathbf{f}}_{\mathbf{i}} \tag{3.39}$$

The time integration scheme starts with the predictor step to compute the intermediate particle positions and densities as follow; $\vec{\mathbf{r}}_{\mathbf{i}}^{(n+1/2)} = \vec{\mathbf{r}}_{\mathbf{i}}^{(n)} + 0.5\vec{\mathbf{v}}_{\mathbf{i}}^{(n)}\Delta t$ and $\rho_{\mathbf{i}}^{(n+1/2)} = \rho_{\mathbf{i}}^{(n)} + 0.5k_{\mathbf{i}}^{(n)}\Delta t$. Having computed the intermediate particle positions and densities during the first half time step, the pressure is computed using the previously introduced artificial equation of state, while the velocity is computed by $\vec{\mathbf{v}}_{\mathbf{i}}^{(n+1)} = \vec{\mathbf{v}}_{\mathbf{i}}^{(n)} + \vec{\mathbf{f}}_{\mathbf{i}}^{(n+1/2)}\Delta t$. In the next half time (the corrector step), the particle positions and densities are updated as $\vec{\mathbf{r}}_{\mathbf{i}}^{(n+1)} = \vec{\mathbf{r}}_{\mathbf{i}}^{(n+1/2)} + 0.5\vec{\mathbf{v}}_{\mathbf{i}}^{(n+1)}\Delta t$, and $\rho_{\mathbf{i}}^{(n+1)} = \rho_{\mathbf{i}}^{(n+1/2)} + 0.5k_{\mathbf{i}}^{(n+1)}\Delta t$, Figure 3-2 summarize the WSPH algorithm.

ISPH approach is based on the projection method [35], which uses the principle of Hodge decomposition. Upon using Hodge decomposition, any vector field can be broken into a divergence-free part plus the gradient of an appropriate scalar potential. Hodge decomposition can be written for a velocity field as $\vec{\mathbf{v}}^{*} = \vec{\mathbf{v}} + \left(\Delta t / \rho\right)\nabla p$, where $\vec{\mathbf{v}}^{*}$ is the intermediate velocity, and $\vec{\mathbf{v}}$ is the divergence-free part of the velocity field. The projection method begins by ignoring the pressure gradient in the momentum balance equation in Equation $(2.1)^{b}$. The solution of Equation $(2.1)^{b}$ without the pressure gradient produces the intermediate velocity $\vec{\mathbf{v}}^{*}$, which does not, in general, satisfy mass conservation. However, this incorrect velocity

field can be projected onto a divergence-free space after solving a pressure Poisson equation, from which the divergence-free part of the velocity field $\vec{\mathbf{v}}$ can be extracted. The pressure Poisson equation is obtained by taking the divergence of $\vec{\mathbf{v}}^* = \vec{\mathbf{v}} + (\Delta t / \rho)\nabla p$ as $\nabla \bullet \vec{\mathbf{v}}^* / \Delta t = \nabla \bullet (\nabla p / \rho)$ since the incompressibility condition requires $\nabla \bullet \vec{\mathbf{v}} = 0$. This equation is subjected to Neumann boundary conditions that can be obtained by using the divergence theorem on the pressure Poisson equation as $(\rho/\Delta t)\vec{\mathbf{v}}^* \bullet \vec{\mathbf{n}} = \nabla p \bullet \vec{\mathbf{n}}$ where $\vec{\mathbf{n}}$ is the unit normal vector. Having solved the pressure Poisson equation to obtain the pressure field and then computed the pressure gradient, we can use the Hodge decomposition equation to determine the correct, incompressible velocity field $\vec{\mathbf{v}}$. One of the main advantage of using ISPH is the elimination of the speed of sound parameter in the time-step conditions. Much larger time steps can be used in this approach, at the computational expense of having to solve the pressure Poisson equation at each time step. The time-step requirement for ISPH is $\Delta t \le C_{CFL} h_{\mathbf{ij},min} / v_{max}$ where in this work, $C_{CFL} = 0.175$. Unlike WSPH, ISPH algorithm does not suffer as much from non-physical pressure fluctuations due to small density errors that may potentially induce numerical instability.

For time marching of ISPH approach, we have used a first-order Euler time step scheme. The general form of the ISPH algorithm is as follow. The predictor step starts with determining an estimate $\vec{\mathbf{r}}_\mathbf{i}^*$ for all particle locations, given the previous particle positions $\vec{\mathbf{r}}_\mathbf{i}^{(n)}$ and the previous correct velocity field $\vec{\mathbf{v}}_\mathbf{i}^{(n)}$ as $\vec{\mathbf{r}}_\mathbf{i}^* = \vec{\mathbf{r}}_\mathbf{i}^{(n)} + \vec{\mathbf{v}}_\mathbf{i}^{(n)} \Delta t$ where $\vec{\mathbf{r}}_\mathbf{i}^*$ is the intermediate particle position. The intermediate velocity field $\vec{\mathbf{v}}_\mathbf{i}^*$ is computed on the temporary particle locations through the solution of the momentum balance equations with forward time integration by omitting the pressure gradient term as $\vec{\mathbf{v}}_\mathbf{i}^* = \vec{\mathbf{v}}_\mathbf{i}^{(n)} + \vec{\mathbf{f}}_\mathbf{i}^{(n)} \Delta t$. The pressure Poisson equation is solved to obtain the pressure $p_\mathbf{i}^{(n+1)}$ which is required to enforce the incompressibility condition. The pressure Poisson equation is solved using a biconjugate gradient stabilized method. The Hodge decomposition principle is employed to solve for the actual velocity field $\vec{\mathbf{v}}_\mathbf{i}^{(n+1)}$ by using the computed pressure $p_\mathbf{i}^{(n+1)}$. Finally, with the correct velocity field for time-step *n+1*, all fluid particles are advected to their new positions $\vec{\mathbf{r}}_\mathbf{i}^{(n+1)}$ using an average of the previous and current

particle velocities as $\vec{\mathbf{r}}_{\mathbf{i}}^{(n+1)} = \vec{\mathbf{r}}_{\mathbf{i}}^{(n)} + 0.5\left(\vec{\mathbf{v}}_{\mathbf{i}}^{(n)} + \vec{\mathbf{v}}_{\mathbf{i}}^{(n+1)}\right)\Delta t$, Figure 3-3 summarize the ISPH algorithm.

3.6 SPH Particles Movement Technique "XSPH"

It is to be noted that in the SPH method, the order of particles affects the accuracy of interpolations for gradient and Laplacian computations. Therefore, for computational stability and accuracy, it is preferable to move the particles in a more orderly fashion, which can be achieved through using XSPH technique suggested by Monaghan et.al [31]. The XSPH method includes the contribution from neighbouring particles, thereby forcing fluid particles to move with an average velocity defined as $\vec{\mathbf{v}}_{\mathbf{i}}^{xsph} = \vec{\mathbf{v}}_{\mathbf{i}} - \varepsilon\sum_{\mathbf{j}=1}^{N}\vec{\mathbf{v}}_{\mathbf{ij}}W\left(r_{\mathbf{ij}},h\right)/\sum_{\mathbf{j}=1}^{N}W\left(r_{\mathbf{ij}},h\right)$, where $\vec{\mathbf{v}}_{\mathbf{ij}} = \left(\vec{\mathbf{v}}_{\mathbf{i}} - \vec{\mathbf{v}}_{\mathbf{j}}\right)$ and ε is a coefficient that varies between zero and 1. In this study, $\vec{\mathbf{v}}_{\mathbf{i}}$ is replaced by the average velocity or XSPH velocity $\vec{\mathbf{v}}_{\mathbf{i}}^{xsph}$ for particle movement only, and $\varepsilon = 0.5$. In all times for both WSPH, and ISPH algorithms, particles are moved with the $\vec{\mathbf{v}}_{\mathbf{i}}^{xsph}$ velocity.

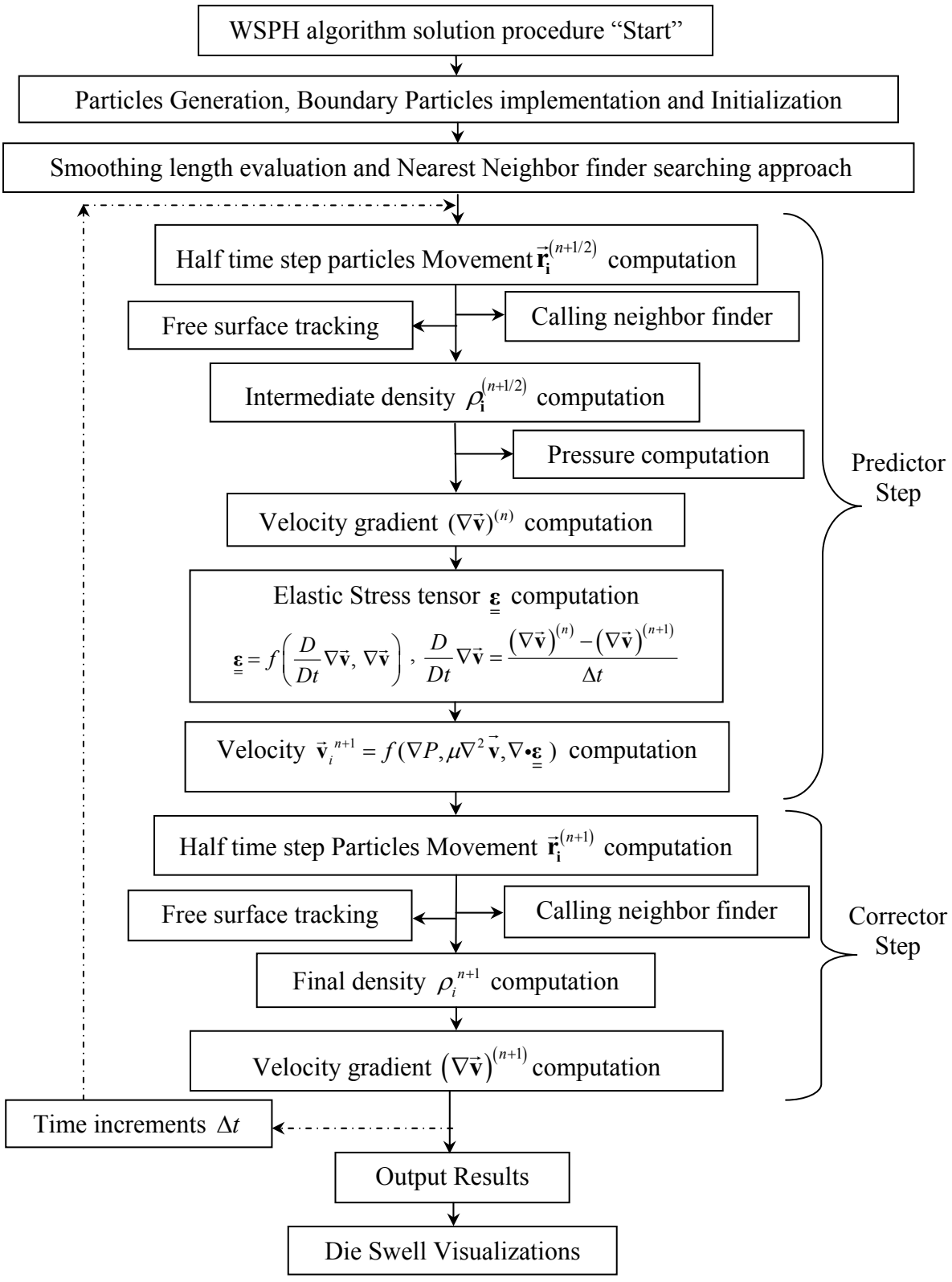

Figure 3-2: Die swell WSPH algorithm solution procedure.

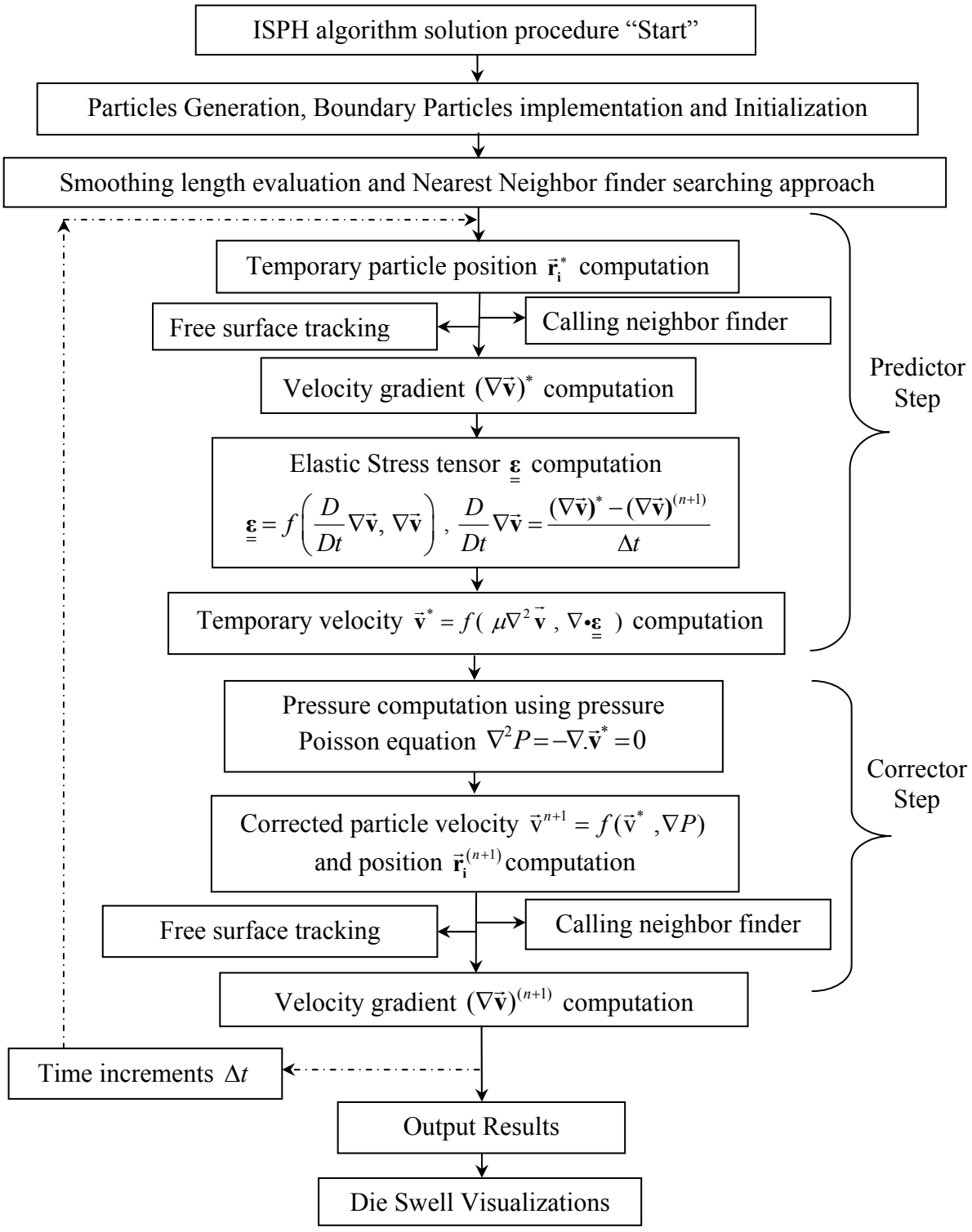

Figure 3-3: Die swell ISPH algorithm solution procedure.

CHAPTER 4

4 DIE SWELL SIMULATION RESULTS BY SPH

4.1 Problem Description for the Die Swell

The simulation domain of the problem in hand is composed of die channel and the extrudate together with their Boundaries, all of which are represented by a set of particles as shown in Figure 4-1. The die channel length and width are 0.2 m. and 0.01 m. respectively as indicated in Figure 4-2. Initially, the simulation domain is represented by 5000 particles generated by using an array of 25 × 200 particles. Henceforth, particles representing solid walls, inlet, outlet, and free surface boundaries are referred to as solid wall boundary particles, die inlet and outlet boundary particles, and free surface boundary particles, respectively. Particles within the die channel as well as the extrudate are named as fluid particles. Particles posses all the essential modelling parameters and field variables such as particle position, velocity, density, viscosity and pressure. Except solid boundary particles, all particles due to the Lagrangian nature of the SPH approach can move and deform freely in accordance with the solution of the mass and linear momentum balance equations.

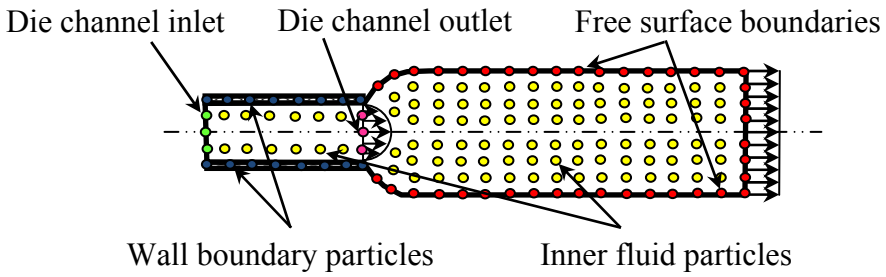

Figure 4-1: The simulation domain in particle representation.

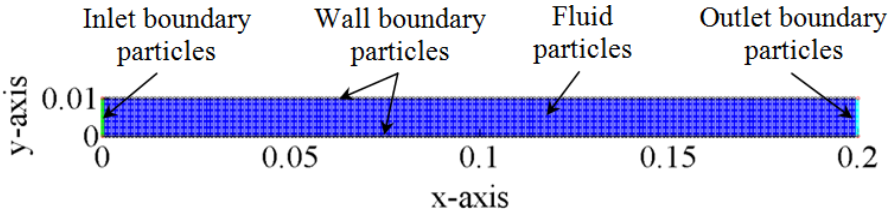

Figure 4-2: The particle distribution on the die channel.

4.2 Die Swell Boundary Conditions

The mass and momentum balance equations on the discontinuity surfaces (boundaries) can be formulated respectively [36] as $\left\|\rho\left(\vec{\mathbf{v}}-\vec{\mathbf{u}}\right)\right\|\bullet\vec{\mathbf{n}}=0$, and $\left\|\rho\vec{\mathbf{v}}\left(\vec{\mathbf{v}}-\vec{\mathbf{u}}\right)-\underline{\underline{\boldsymbol{\sigma}}}\right\|\bullet\vec{\mathbf{n}}=\nabla_{(s)}\gamma+2\Gamma\gamma\vec{\mathbf{n}}$. Here, the symbol $\left\|\ \right\|$ indicates the jump of the enclosed quantities across the discontinuity surface; for instance, $\left\|\varphi\right\|=\varphi^{+}-\varphi^{-}$ where φ^{+} and φ^{-} are the values of φ on the positive and negative sides of the discontinuity surface, $\vec{\mathbf{u}}$ is the velocity of the discontinuity surface, $\vec{\mathbf{n}}$ is the unit normal to the discontinuity surface, $\nabla_{(s)}$ is the surface gradient operator, γ is the surface tension, Γ is the mean curvature. Under the assumptions of no-slip and no-mass penetration boundary conditions for rigid solid walls, the interface mass balance requires that $v_x=v_y=0$. Also assuming no mass penetration across free surfaces as well as ignoring the effect of surface tension, one can reduce the jump condition of the linear momentum balance to

$\left\|\underline{\underline{\boldsymbol{\sigma}}}\right\|\cdot\vec{\mathbf{n}}=0$ where $\underline{\underline{\boldsymbol{\sigma}}}=-p\underline{\underline{\mathbf{I}}}+\underline{\underline{\mathbf{T}}}$. Since the problem in question is the flow of highly viscous fluid into a passive environment with comparatively low viscosity and zero pressure, the free surface boundary condition $\left\|\underline{\underline{\boldsymbol{\sigma}}}\right\|\cdot\vec{\mathbf{n}}=0$ is modified to $\underline{\underline{\mathbf{T}}}\cdot\vec{\mathbf{n}}=0$, whereby implying zero pressure and the stress free boundary condition for the free surface .

The domain boundaries truncate the kernel function of particles which are on or close to the boundaries. Hence, only interior particles will contribute to the SPH approximation for these particles due to the lack of interpolation points on the other side of the boundary. The standard SPH equations introduced in the preceding sections, being valid for all interior particles, are partially correct since the kernel function for these particles is no longer a normalized, compact and spherically symmetric even function. Therefore, the application of boundary conditions correctly and efficiently is quite challenging in the SPH method, and necessitates special treatments depending on the type of the boundary. Inaccurate implementation of boundary conditions for example results in the penetration of fluid particles into boundary walls, and may lead to spurious gradients of field variables whereby producing errors in the solution since the field variables within the computational domain evolve according to the boundary conditions. In this direction, over the last decade, several different approaches have been suggested to improve boundary treatments which are systematically summarized in various works [19, 21, 23, 33].

Within the context of the SPH method, the solid wall boundaries can be represented by a set of particles. The no-slip boundary conditions on solid boundary walls can be easily implemented by fixing the positions of wall boundary particles and setting their velocities to zero throughout the simulation. In our simulations, we have observed that single layer of wall boundary particles is not sufficient to compute the field variables accurately such as stress, velocity, and pressure; hence, additional layers of solid dummy boundary particles are created parallel to the main wall boundary particles. The overall thickness of these dummy particle layers is set to be at least equal to the radius of the kernel smoothing function. The existence of dummy wall particles help reducing the error in computed fields due to the kernel truncation by boundaries. Dummy boundary particles are assigned to zero velocity as well. Both wall boundary and dummy particles behave similar to fluid particles such that their

density and extra stress tensors are computed using the discretization scheme in Equation (3.16).

As for the implementation of boundary conditions for the free surface, firstly, the free surface particles should be identified to distinguish them from interior fluid particles. Since the kernel function of particles that are on or in the close vicinity of the free surface is truncated; the particle number density $n_{\mathbf{i}}$ for these particles will drop. Particles with the number densities below a preset threshold value are recognized as free surface particles: namely, $n_{\mathbf{i}} \le 0.8 n_{\mathbf{i},\,ref}$, where the number density is computed as $n_{\mathbf{i}} = \sum_{\mathbf{j}=1}^{N} W\left(r_{\mathbf{ij}}, h\right)$ and $n_{\mathbf{i},\,ref} = \max\left(n_{\mathbf{i}}\right)$. In SPH modelling, the stress free boundary condition $\underline{\underline{\mathbf{T}}} \bullet \vec{\mathbf{n}} = 0$ is automatically satisfied since in evaluating the stress gradient in momentum equation, this term is represented in the residual boundary integration which is cancelled due to the fact that kernel function $W\left(r_{\mathbf{ij}}, h\right)$ vanishes beyond its support domain as shown in Equation (3.6). Due to the lack of interpolation points or particles outside the free surface, the pressure field computed for the free surface particles can be affected significantly by the spurious pressure gradient. To improve the accuracy of the computed pressure fields, pressure gradients for free surface particles are computed through assuming the existence of dummy fluid particles $\mathbf{j}^d$ outside the free surface, which are mirror images of associated interior fluid particles $\mathbf{j}^f$ as shown in Figure 4-3.

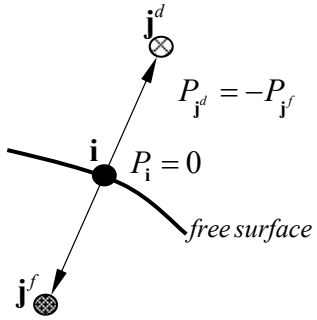

Figure 4-3: A schematic for enforcing zero pressure condition on the free surface.

In what follows, one can write

$$\frac{\partial P}{\partial x_{\mathbf{i}}^k} = \sum_{\mathbf{j}=1}^{N} \frac{m_{\mathbf{j}}}{\rho_{\mathbf{j}}} \left(P_{\mathbf{j}^d} - P_{\mathbf{i}}\right) \frac{\partial W\left(r_{\mathbf{ij}^d}, h\right)}{\partial x_{\mathbf{i}}^k} + \sum_{\mathbf{j}=1}^{N} \frac{m_{\mathbf{j}}}{\rho_{\mathbf{j}}} \left(P_{\mathbf{j}^f} - P_{\mathbf{i}}\right) \frac{\partial W\left(r_{\mathbf{ij}^f}, h\right)}{\partial x_{\mathbf{i}}^k} = 2 \sum_{\mathbf{j}=1}^{N} \frac{m_{\mathbf{j}}}{\rho_{\mathbf{j}}} P_{\mathbf{j}^f} \frac{\partial W\left(r_{\mathbf{ij}^f}, h\right)}{\partial x_{\mathbf{i}}^k} \tag{4.1}$$

where $\partial W\left(r_{\mathbf{ij}^d},h\right)/\partial x_{\mathbf{i}}^k=-\partial W\left(r_{\mathbf{ij}^f},h\right)/\partial x_{\mathbf{i}}^k$, $P_{\mathbf{i}}=0$, and $P_{\mathbf{j}^d}=-P_{\mathbf{j}^f}$ which enforce zero pressure boundary condition.

4.3 Periodic Channel Flow

This section aims at validating the numerical results obtained by the SPH method presented. Therefore, we present two benchmark problems including both Newtonian and non-Newtonian Poiseuille flows. Poiseuille flow consists of two infinitely long stationary plates, parallel to the *x*-axis, with a fluid in between them. These plates are separated by a distance H, where $y = 0$ is the position of the bottom plate, and $y = H$ is the position of the top plate. At time $t = 0$, a body force F_x^B is applied to the fluid acting in the *x*-direction, thereby putting the fluid in motion $v_x=v_x\left(y,t\right)$. The no-slip boundary conditions are employed at the plate/fluid interfaces $y=0$ and $y = H$, so that $v_x\left(0,t\right)=v_x\left(H,t\right)=0$. The initial condition for all interior particles is taken as $v_x\left(y,0\right)=0$.

4.3.1 Newtonian Poiseuille Flow

For Newtonian incompressible Poiseuille flow, the governing flow equation is the one-dimensional balance of linear momentum equation, $\rho\dot{v}_x=-p_{,x}+\mu\left(\tau_{xx,x}+\tau_{yx,y}\right)+\rho F_x^B$, which can be reduced to $\rho\dot{v}_x=-p_{,x}+\mu v_{x,yy}+\rho F_x^B$ assuming no variation of v_x in the *x*-direction and noting that $\tau_{xx}=0$ and $\tau_{yx}=\mu v_{x,y}$. A body force F_x^B is used to model the hydrostatic part of the pressure gradient. To initiate the modelling process, a 30×70 array of particles distributed in x- and y-directions, respectively, were created in the domain, and the modelling parameters were taken as $H=10^{-3}m$, $L=5\text{x}10^{-4}m$, $F_x^B=2\text{x}10^{-4}N/kg$, $\rho=1000\,kg/m^3$ and $\mu=10^{-3}\,Pa\,s$. The smoothing length was set equal to 1.6 times the biggest initial particle

spacing. The periodic boundary condition is applied for inlet and outlet particles in the direction of the flow. In the WSPH simulation of a periodic channel flow in literature, the periodic boundary condition is in general imposed such that fluid particles crossing the outlet boundary are reinserted into flow domain at the same y-coordinate with the same velocity and density. However, for a relatively long channel, a noticeable pressure loss can be observed along the channel length. In WSPH, since the pressure field is computed from the density using an artificial equation of state, the outlet boundary pressure poisons the inlet boundary. To circumvent this, the outlet particles are inserted into the flow domain with the same density gradient as at the outlet using the Equation (4.2)

$$\rho_{\mathbf{i}} = \left[\sum_{\mathbf{j}=1}^{N} \frac{m_{\mathbf{j}}}{\rho_{\mathbf{j}}} \rho_{\mathbf{j}} \frac{\partial W\left(r_{\mathbf{ij}}, h\right)}{\partial x_{\mathbf{i}}} - \left(\frac{\partial \rho_{\mathbf{i}}}{\partial x_{\mathbf{i}}} \right)_{out} \right] / \sum_{\mathbf{j}=1}^{N} \frac{m_{\mathbf{j}}}{\rho_{\mathbf{j}}} \frac{\partial W\left(r_{\mathbf{ij}}, h\right)}{\partial x_{\mathbf{i}}} \tag{4.2}$$

An analytical solution to the transient velocity profile for the incompressible Poiseuille flow can be written as [21],

$$v_x(y,t) = \frac{4\rho F_x^B H^2}{\mu\pi^3} \sum_{k=0}^{\infty} \frac{1}{(2k+1)^3} \sin\left[\frac{(2k+1)\pi y}{H} \right] \exp\left[\frac{-(2k+1)^2 \mu\pi^2 t}{\rho H^2} \right] + \frac{\rho F_x^B}{2\mu} y(y-H) \tag{4.3}$$

which takes on a parabolic velocity profile as $t \to \infty$.

Figure 4-4 illustrates the SPH and analytical transient solutions to the Poiseuille flow problem at various times.

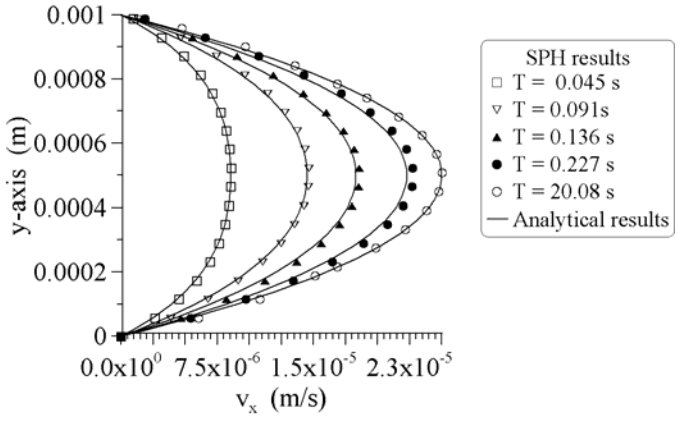

Figure 4-4: Newtonian incompressible Poiseuille flow velocity profile at the middle of the channel.

4.3.2 Non-Newtonian Poiseuille Flow

The second test fluid flow problem involves a simulation of one-dimensional, steady state non-Newtonian incompressible Poiseuille flow. As a constitutive equation, we have used Rivlin-Ericksen tensor along with the contravariant form of the convected time derivative. The extra stress tensor of this form can be written in a component form as

$$T_{ij}\vec{e}_i\vec{e}_j = \left\{ \begin{array}{l} \mu\left[v_{j`i}+v_{i`j}\right]+\alpha_1\left(\dfrac{D}{Dt}\left[v_{j`i}+v_{i`j}\right]-2v_{i`m}v_{j`m}-v_{i`m}v_{m`j}-v_{m`i}v_{j`m}\right) \\ +\alpha_2\left(v_{m`i}v_{j`m}+v_{m`i}v_{m`j}+v_{i`m}v_{j`m}+v_{i`m}v_{m`j}\right) \end{array} \right\}\vec{e}_i\vec{e}_j \qquad (4.4)$$

Equation (4.4) can be further simplified to the following open forms after using the summation convention and imposing incompressibility condition as,

$$\begin{aligned} T_{xx} &= 2\mu v_{x,x}+\alpha_1\left(2Dv_{x,x}/Dt-4v_{x,x}^2-2v_{x,y}^2-2v_{x,y}v_{y,x}\right) \\ &\quad +\alpha_2\left(4v_{x,x}^2+2v_{x,y}v_{y,x}+v_{y,x}^2+v_{x,y}^2\right) \end{aligned} \qquad (4.5)$$

$$T_{xy} = \mu\left(v_{y,x}+v_{x,y}\right)+\alpha_1\left(D\left(v_{y,x}+v_{x,y}\right)/Dt-2v_{x,x}v_{y,x}-2v_{x,y}v_{y,y}\right) \qquad (4.6)$$

$$\begin{aligned} T_{yy} &= 2\mu v_{y,y}+\alpha_1\left(2Dv_{y,y}/Dt-4v_{y,y}^2-2v_{y,x}^2-2v_{y,x}v_{x,y}\right) \\ &\quad +\alpha_2\left(4v_{y,y}^2+2v_{y,x}v_{x,y}+v_{x,y}^2+v_{y,x}^2\right) \end{aligned} \qquad (4.7)$$

Casting Equations (4.5), (4.6), and (4.7) into the momentum balance in Equation (2.1)[b] , the x - and y - components of the balance of linear momentum can be written as

$$\rho\frac{Dv_x}{Dt} = \left\{ \begin{array}{l} -p_{,x}+\mu\left(v_{x,xx}+v_{x,yy}\right) \\ +\alpha_1\left(\begin{array}{l} D\left(v_{x,xx}+v_{x,yy}\right)/Dt-8v_{x,x}v_{x,xx}-4v_{x,y}v_{x,xy}-4v_{y,x}v_{x,xy} \\ -2v_{x,x}v_{y,yx}-2v_{y,y}v_{x,yy}-2v_{x,y}v_{y,yy}-2v_{x,y}v_{y,xx} \end{array}\right) \\ +\alpha_2\left(8v_{x,x}v_{x,xx}+2v_{x,y}v_{y,xx}+2v_{y,x}v_{x,xy}+2v_{x,y}v_{x,xy}+2v_{y,x}v_{y,xx}\right) \end{array} \right\}+\rho F_x^B \qquad (4.8)$$

$$\rho\frac{Dv_y}{Dt}=\begin{Bmatrix} -p_{,y}+\mu\left(v_{y,xx}+v_{y,yy}\right) \\ +\alpha_1\begin{pmatrix} D\left(v_{y,xx}+v_{y,yy}\right)/Dt-8v_{y,y}v_{y,yy}-4v_{y,x}v_{y,yx}-4v_{x,y}v_{y,yx} \\ -2v_{y,x}v_{x,xx}-2v_{x,x}v_{y,xx}-2v_{y,y}v_{x,xy}-2v_{y,x}v_{x,yy} \end{pmatrix} \\ +\alpha_2\left(8v_{y,y}v_{y,yy}+2v_{y,x}v_{x,yy}+2v_{x,y}v_{y,yx}+2v_{x,y}v_{x,yy}+2v_{y,x}v_{y,yx}\right) \end{Bmatrix} \tag{4.9}$$

The one-dimensional steady state governing equation can be obtained from Equation (4.8) as $\mu v_{x,yy}=\rho F_x^B$ where no variation of v_x and p in the x-direction is assumed. Upon implementing the no slip boundary conditions at the plate/fluid interfaces, the fully developed velocity profile can be obtained as $v_x(y)=-4\mathrm{v}_{\max}\left(y^2/H^2-y/H\right)$ where $\mathrm{v}_{\max}$ is the centerline velocity, and defined to be $\mathrm{v}_{\max}=-\rho F_x^B H^2/8\mu$. The components of the extra stress tensor can be obtained as $T_{xx}=\left(\alpha_2-2\alpha_1\right)v_{x,y}^2$, and $T_{xy}=\mu\left(v_{x,y}\right)$ from Equations (4.5) and (4.6), respectively. The computational domain is formed by a 300×33 array of particles distributed in x- and y-directions, respectively. The smoothing length was set equal to 1.6 times the initial particle spacing. The simulation is performed with the following input parameters; H=0.01 m, L=0.2 m, $F_x^B=3200\ N/kg$ $\rho=1000\,kg/m^3$, $\mu=10$ Pa s, $\alpha_1=-2\mathrm{x}10^{-3}$ Pa s^2, and $\alpha_2=-0.1$ x α_1 which produces a center line velocity of 3.6 m/s, and Deborah number of 0.072. In this test problem, we also used periodic boundary conditions at the inlet and outlet boundaries.

Figure 4-5 presents the SPH and steady state analytical solutions for the velocity magnitude v, T_{xx}, and T_{xy} at the channel length of *x=0.1* m. The comparison of SPH and analytical results shows good agreement, and one therefore can conclude that SPH method can capture the flow behaviour of a second order fluid very well.

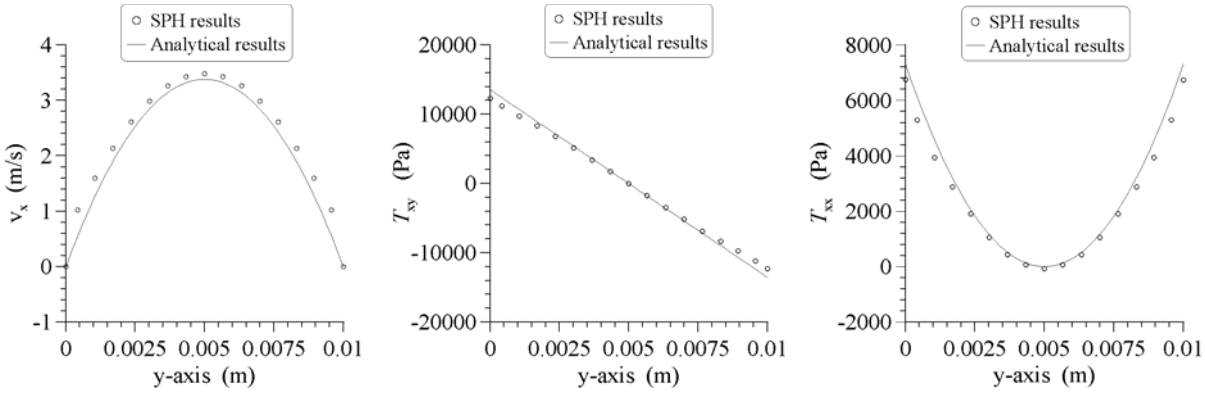

(a) velocity profile (b) T_{xy} profile (c) T_{xx} profile

Figure 4-5: Fully developed non-Newtonian second-order periodic flow.

4.4 Simulation Results for the Extrudate Swell

This section presents the simulation results of a two-dimensional transient die swell problem under several operating parameters and for various forms of discretization schemes as well as for different formulations of constitutive equations. The model domain and its geometrical parameters have been introduced previously in section 4.1. The fluid parameters ρ =1000 kg/m^3, $\mu = 10$ Pa s are selected for whole simulations. As stated before, the die swell problem was studied using both the WSPH and the ISPH approaches. Nevertheless, the majority of the results presented here have been produced using the WSPH algorithm unless stated otherwise. The initial conditions for all interior fluid particles are taken as zero initial velocities. Fluid particles are accelerated from rest upon the application of a constant body force as described in the benchmark problems. Body force is applied only to fluid particles within the channel. Upon crossing the die channel outlet boundary, fluid particles start moving and deforming freely under the influence of upstream fluid particles.

4.4.1 Different Forms of Momentum Balance Equation

As emphasized in Chapter 2 of the present study, the literature review has shown that there is not a well-established consensus or a guideline regarding the form of a constitutive equation that can be used to model the die swell behaviour of non-Newtonian visco-elastic second order fluid in extrusion process. In the relevant documented literature, mainly two different constitutive equations and four different forms of convected derivatives are reported, thereby producing eight possible forms of the momentum balance equation. In the following, we present the findings of a systematic study on the ability of each possible form to predict the die swell phenomenon in an extrusion process. To achieve one to one comparison among all simulation results, the same input parameters are used in each momentum equation. Input parameters are body force F_x^B = 18800.0 m/s^2, first and second normal stresses coefficients, $\alpha_1 = -4.0\text{x}10^{-3}$ Pa s^2 and, $\alpha_2 = -0.1$ x α_1. In Figure 4-6 is shown the SPH particle distribution both within the die and extrudate obtained through the solution of eight possible forms of the momentum balance equations. Colors indicate the values of the first normal stress difference N_1 within the channel and the extrudate. When results in Figure 4-6 are compared against each other, it turns out that the momentum balance equation constructed using the Rivlin-Erickson tensor together with the contravariant components of the convected derivative is able to capture the swelling phenomenon satisfactorily, whereas the remaining equations can not predict a correct trend. Hence, the momentum equation due to "***Ab***" combination was chosen to be a default momentum equation for the benchmark problem already introduced as well as for all other die swell simulations to be presented in coming sections.

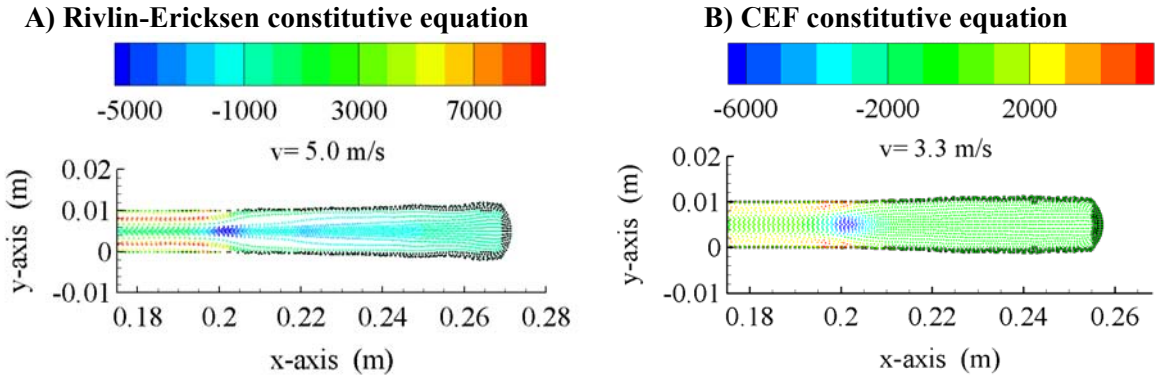

a) Covariant convected derivative.

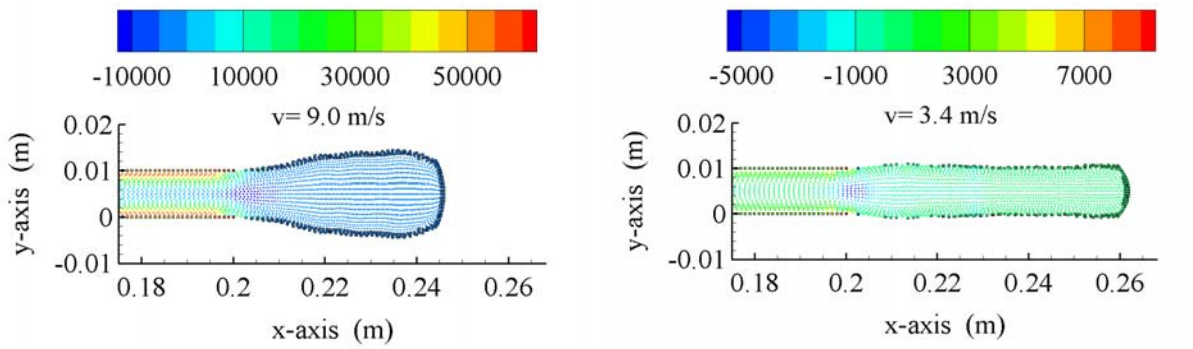

b) Contravariant convected derivative.

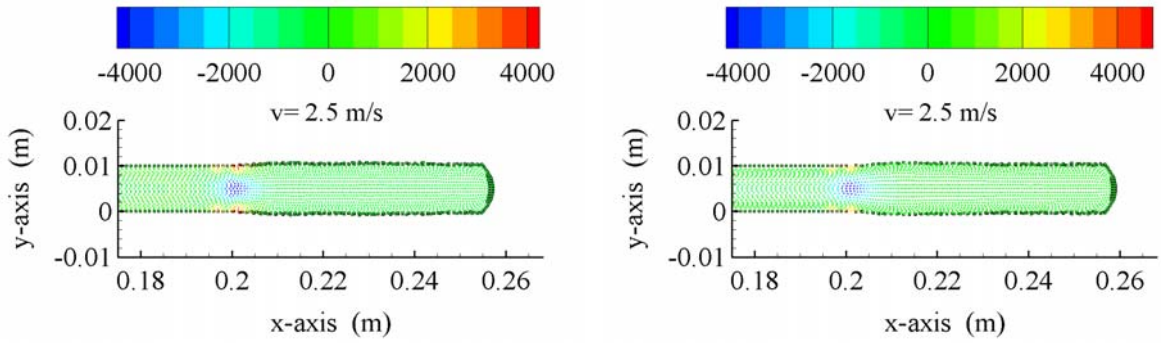

c) Mixed covariant-contravariant convected derivative.

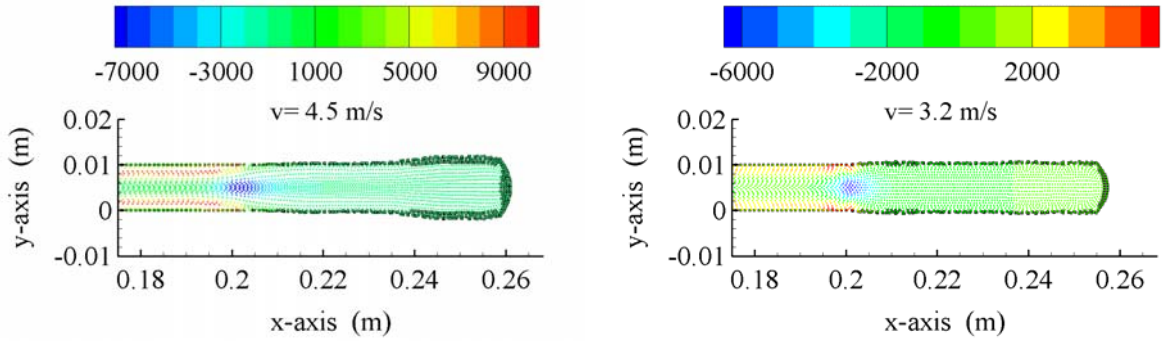

d) Corotational (Jaumann) derivative.

Figure 4-6: SPH particle distribution for eight possible forms of momentum balance formulations. Note that in each figure, the particles distribution are coloured in accordance with the values of the first normal stress difference N_1, and the magnitude of the centerline velocity v is given on each subfigures.

4.4.2 Two Steps and One Step Solution Methodology

In an attempt to find a correct methodology for solving the linear momentum balance equation of a second order fluid, we have tested four solution procedures which differ from each other

in terms of the discretization schemes used and whether the divergence of total stress tensor $\underline{\underline{\boldsymbol{\sigma}}}$, extra stress tensor $\underline{\underline{\mathbf{T}}}$, viscous stress tensor $\underline{\underline{\boldsymbol{\tau}}}$, or elastic stress tensor $\underline{\underline{\boldsymbol{\varepsilon}}}$ are computed in a single-step (loop) or in two-steps. In all two-step methodologies, initially, the components of the velocity gradient are computed using Equation (3.16).

- **Case1**: having computed the total stress tensor $\underline{\underline{\boldsymbol{\sigma}}} = -p\underline{\underline{\mathbf{I}}} + \underline{\underline{\boldsymbol{\tau}}} + \underline{\underline{\boldsymbol{\varepsilon}}}$ in the first step, the divergence of the total stress tensor is computed using Equation (3.18) in the second step.

- **Case2:** after computing the extra stress tensor in the first step, the gradient of the hydrostatic part of the total stress tensor is obtained using Equation (3.16), while the divergence of the extra stress tensor $\underline{\underline{\mathbf{T}}}$ is calculated by using Equation (3.18) in the second step.

- **Case3:** all three parts of the total stress tensor evaluated individually, where ∇p is evaluated with Equation (3.16), $\nabla \bullet \underline{\underline{\boldsymbol{\tau}}}$ is evaluated as a Laplacian term using Equation (3.37) in a single-step, and finally, $\nabla \bullet \underline{\underline{\boldsymbol{\varepsilon}}}$ is computed with Equation (3.18) in the second step after the computation of elastic part $\underline{\underline{\boldsymbol{\varepsilon}}}$ during the first step.

- **Case4:** this is a single-step procedure where each of the first and the second order derivatives in Equations (4.8) and (4.9) are individually evaluated using Equations (3.16) and (3.36).

All four cases have been tested under the same input parameters; namely, the magnitude of the centerline velocity $\mathrm{v} \cong 3.4$ m/s, $\alpha_1 = -2.8 \times 10^{-3}\ \mathrm{Pa}\, s^2$, and $\alpha_2 = -0.1 \times \alpha_1$, which produces $De = 0.0952$. The results of all relevant simulations led us to conclude that **Case1** and **Case2** procedures could not predict the correct flow behaviour in that fluid particles gradually become unstable especially outside the channel as the simulation progress. On the other hand, **Case3** and **Case4** result in stable simulations as shown in Figure 4-7 and Figure 4-8.

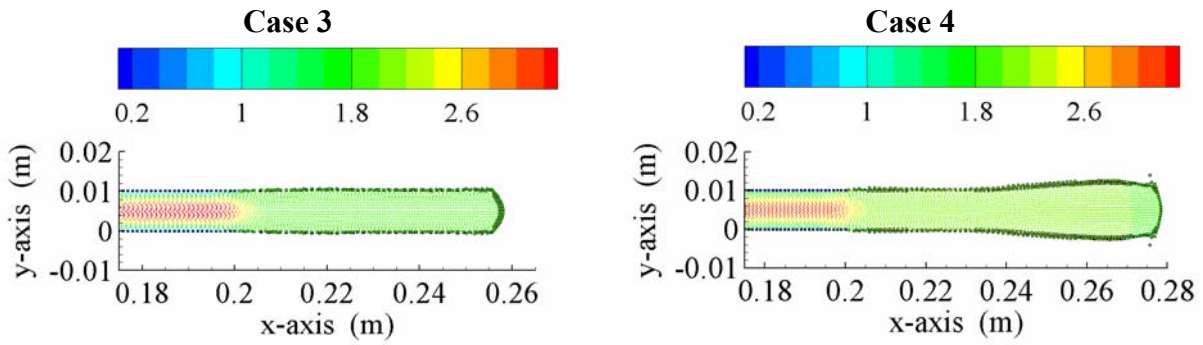

a) the magnitude of the velocity, *m/s*

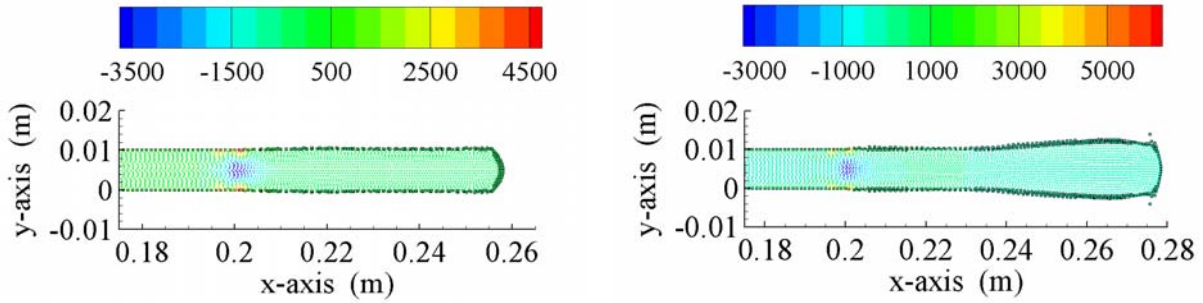

b) the normal component T_{xx} of the extra stress tensor in the *x*-direction, *Pa*.

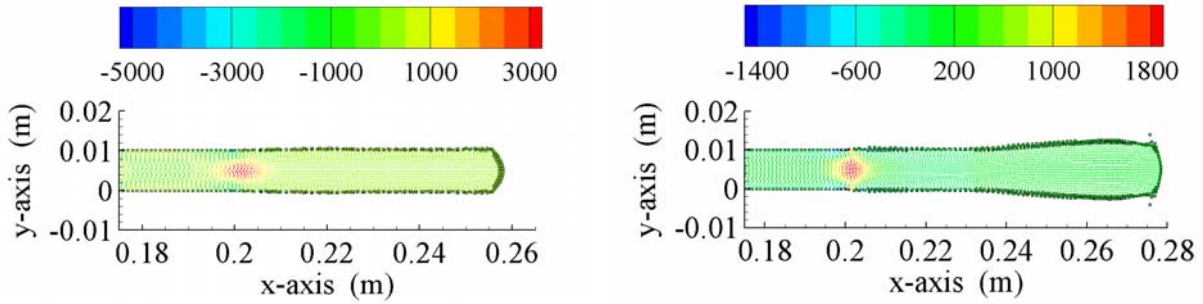

c) the normal component T_{yy} of the extra stress tensor in the y-direction, *Pa*.

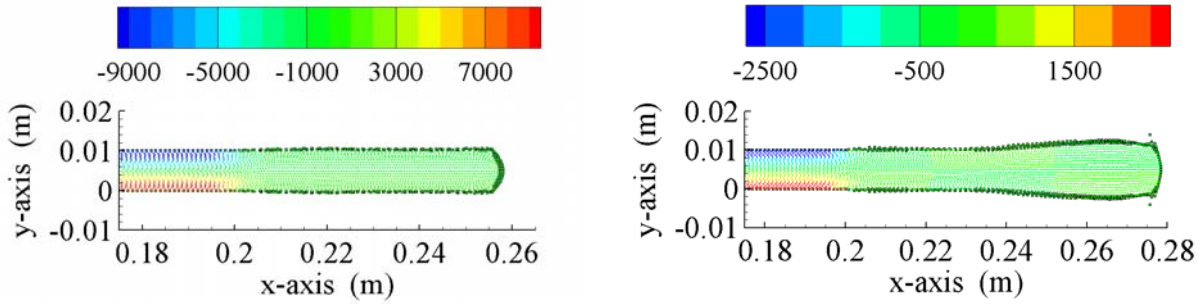

d) the shear component T_{xy} of extra stress tensor stress, *Pa*.

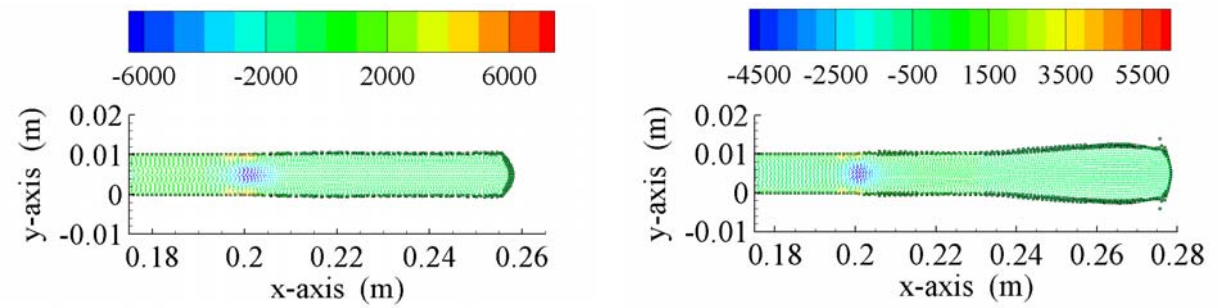

e) the first normal stress difference N_1, *Pa.*

Figure 4-7: Simulation results for Case3 and Case4.

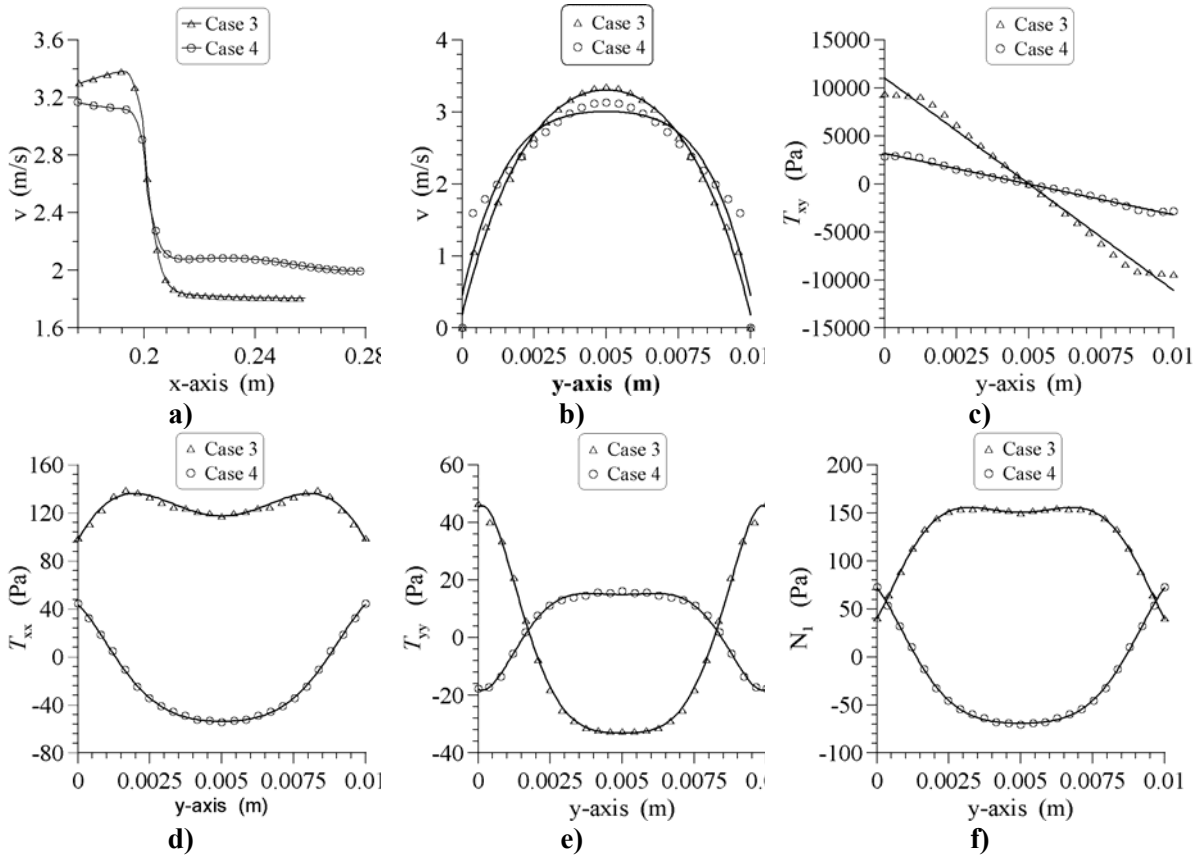

Figure 4-8: a) Magnitude of the velocity versus the axial distance, b) magnitude of the velocity as a function of channel width, c) the shear component T_{xy} of the extra stress tensor, d) the normal component T_{xx} of the extra stress tensor in the *x*-direction, e) the normal component T_{yy} of the extra stress tensor in the y-direction, and f) the first normal stress difference N_1. Results are shown for *x*= 0.185 m.

Simulation results have revealed that the **Case4** procedure seems to capture the swelling phenomenon; nevertheless, it is rather sensitive to the magnitude of the De number, and only works for quite small De number values with the upper bound of 0.0952, above which the fluid flow gets highly instable producing oscillating and perturbed free surface. As well, **Case4**, does not produce the correct fields. The approach presented in **Case3** proves to be the most applicable and effective one in capturing swelling process. Since the De number used in this set of simulations is rather small, the polymeric fluid did not exhibit noticeable die swell upon being extruded.

4.4.3 The First and the Second Normal Stress Coefficients Effects

The first and the second normal stress coefficients have a significant influence on the behaviour of extruded fluid flow. It is important to note that the sign of the first normal stress coefficient α_1 determines whether the polymeric fluid swells or contracts upon being extruded. For swelling phenomenon to occur, the first normal stress coefficient should be of a negative sign leading to positive $N_1 > 0$, while the positive first normal stress coefficient results in negative $N_1 < 0$, hence forcing the polymeric fluid to contract. To be able to test if the developed algorithm can also predict the contraction behaviour, we have performed comparative numerical simulation studies with the following input parameters; for simulating swelling process, $\alpha_1 = -4.0\text{x}10^{-3}$ Pa s^2, $\alpha_2 = -0.1$ x α_1, and $F_x^B = 18800\ N/kg$, while for the contraction phenomenon, $\alpha_1 = 4.0\text{x}10^{-3}$ Pa s^2, $\alpha_2 = -0.1$ x α_1, and $F_x^B = 200000\ N/kg$. These parameters produce a center line velocity of $\text{v} \cong 9.0$ m/s, resulting in $De = 0.38$.

The extrudate contraction **The extrudate swelling**

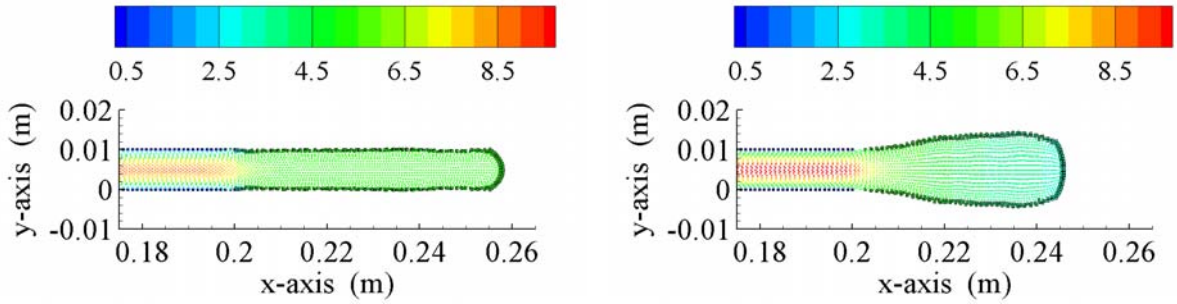

a) the magnitude of the velocity, *m/s*.

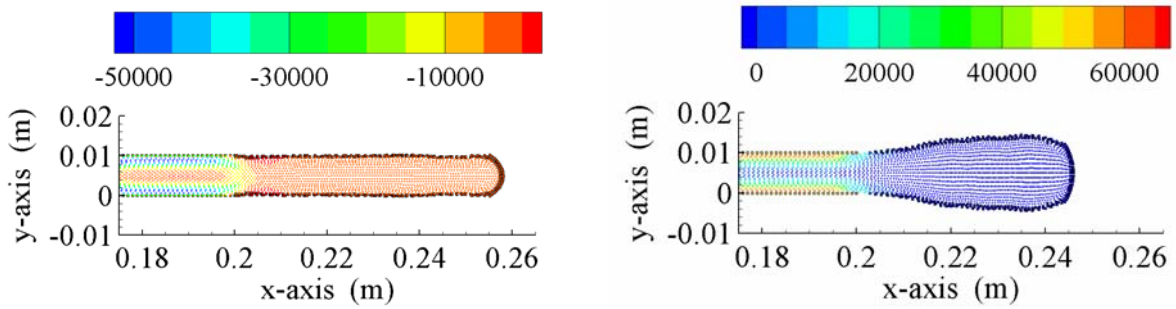

b) the normal component T_{xx} of the extra stress tensor in the *x*-direction, *Pa.*

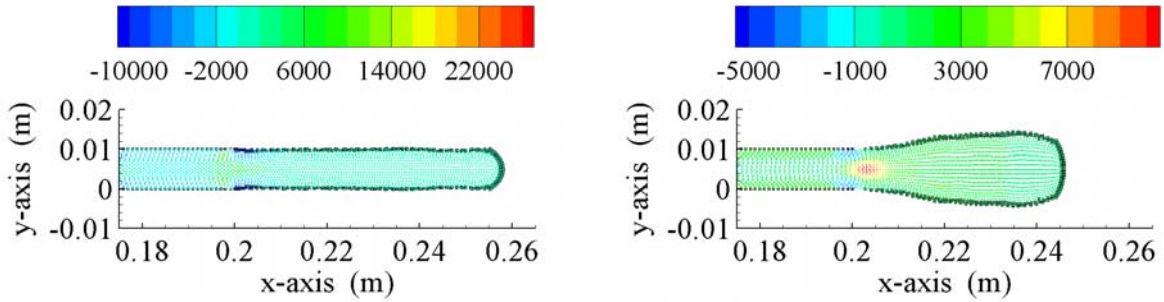

c) the normal component T_{yy} of the extra stress tensor in the y-direction, *Pa*.

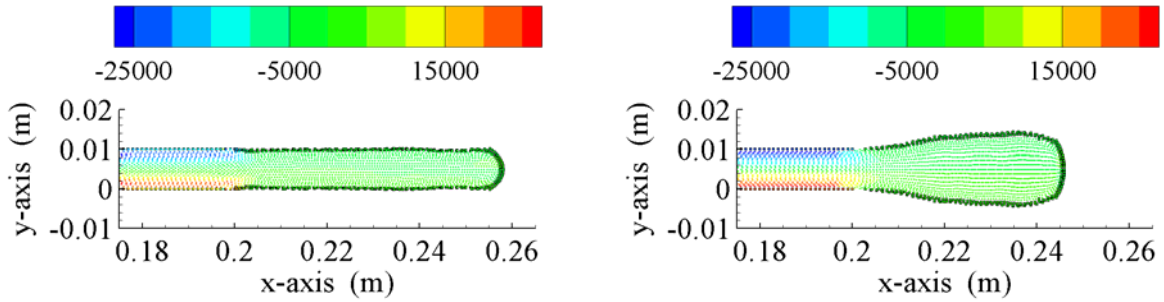

d) the shear component T_{xy} of extra stress tensor stress, *Pa.*

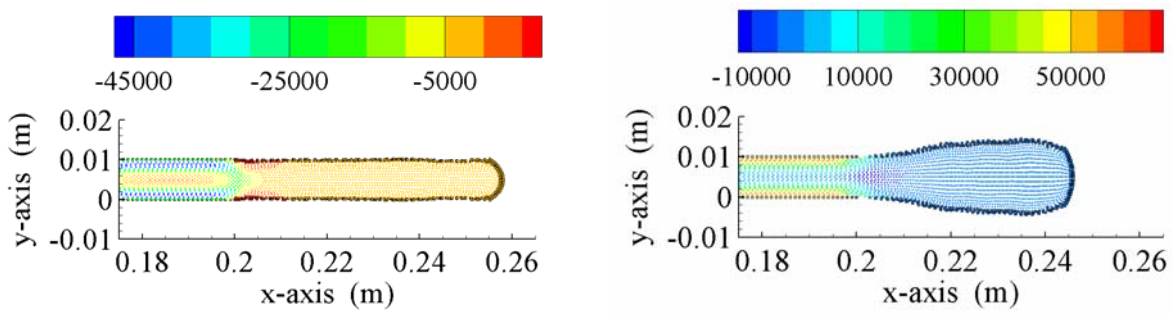

e) the first normal stress difference N_1, *Pa.*

Figure 4-9: Simulation results for the extrudate contraction and swelling.

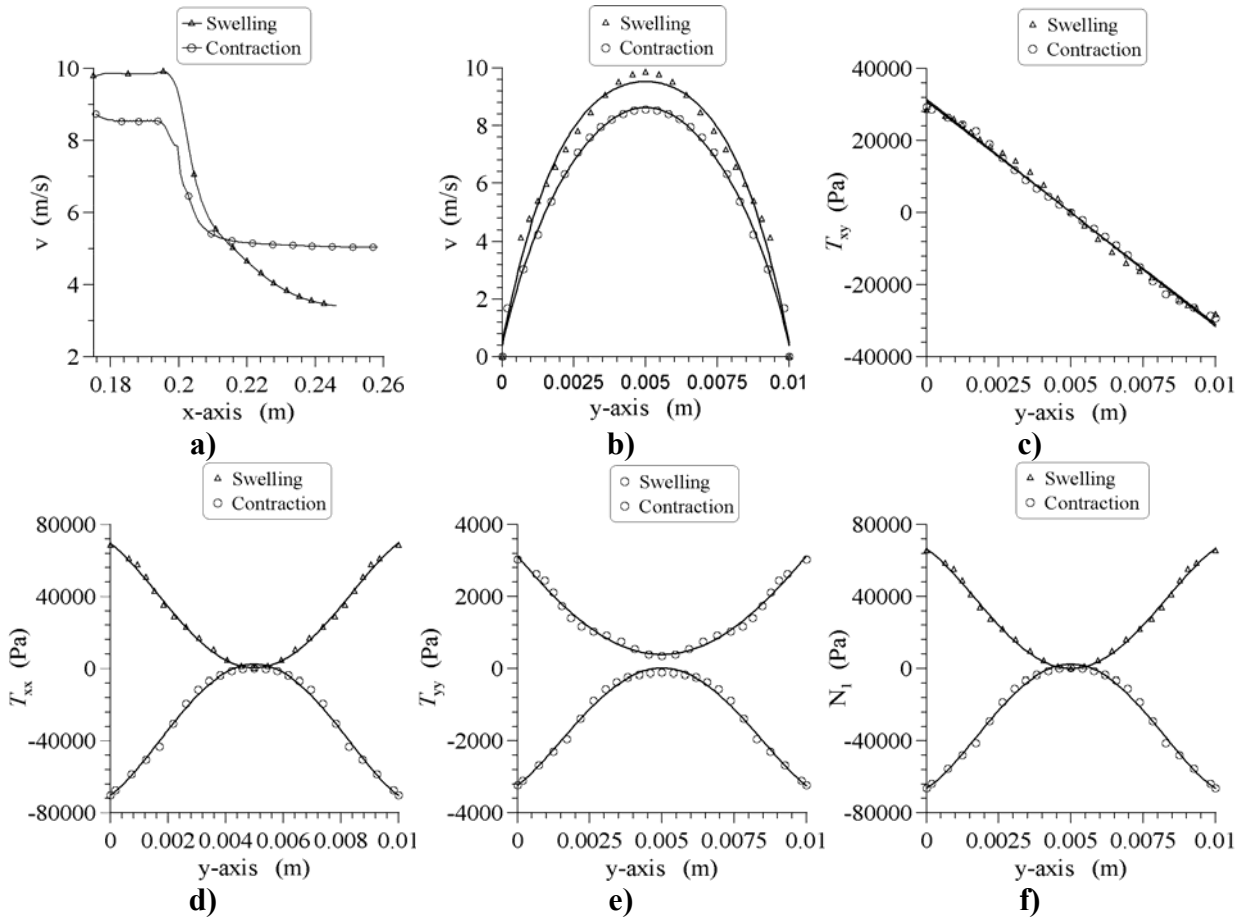

Figure 4-10: a) Magnitude of the velocity versus the axial distance, b) magnitude of the velocity as a function of channel width, c) the shear component T_{xy} of the extra stress tensor, d) the normal component T_{xx} of the extra stress tensor in the *x*-direction, e) the normal component T_{yy} of the extra stress tensor in the y-direction, and f) the first normal stress difference N_1. Results are shown for *x*= 0.185 m. Recalling that since a body force is used to accelerate the

fluid particles, it is difficult to fine-tune the applied body force such that an identical centerline velocity for contraction and swelling phenomena can be produced.

Figure 4-9 and Figure 4-10 present the simulation results for both swelling and contraction cases. One can safely conclude that die swell or contraction is a flow phenomena observed in a viscoelastic fluid. When a polymeric fluid is sheared between the walls of the die, it develops tensile stresses along the flow direction (positive T_{xx}) bringing about positive first normal stress difference $N_1 > 0$. This additional stress in the fluid exerts a net force on the walls of the channel. Once the polymeric fluid is extruded through the die, it can not support this additional stress; hence the fluid tends to expand in the radial direction. On the other hand, some other polymeric fluids when sheared may develop compression along the streamlines (negative T_{xx}), thereby resulting in negative $N_1 < 0$. Hence, normal stresses are responsible for the occurrence of polymer swelling and contraction. An interesting observation to note is that to achieve the same centerline velocity, the body force applied in the simulation of the contraction phenomenon is higher than that used in the swelling case. This is due to the fact that since the fluid element is compressed along the stream line direction (negative T_{xx}), the body force applied is used for overcoming this compression and keeping the flow in motion.

4.4.4 Inlet Velocity Effects on the Extrudate Swell

To study the effect of velocity on the extrudate swelling, we performed two numerical experiments with the same viscometric parameters, $\alpha_1 = -4.0 \times 10^{-3}$ Pa s^2, $\alpha_2 = -0.1 \times \alpha_1$. The fluid is accelerated with the body force of $F_x^B = 11000\, N/kg$ for the first experiment, and $F_x^B = 18800\ N/kg$ for the second experiment. The computed center line velocity magnitudes and Deborah numbers for each experiment are $v \cong 2$ m/s and $De = 0.08$, and $v \cong 10$ m/s and $De = 0.4$, respectively. It is obvious from Figure 4-11 and Figure 4-12 that the raise in the extrusion velocity increases the shear rate. Remembering that the first normal stress difference

is a function of the shear rate, as the shear rate increases, so does the normal stress difference, and in turn swelling is augmented.

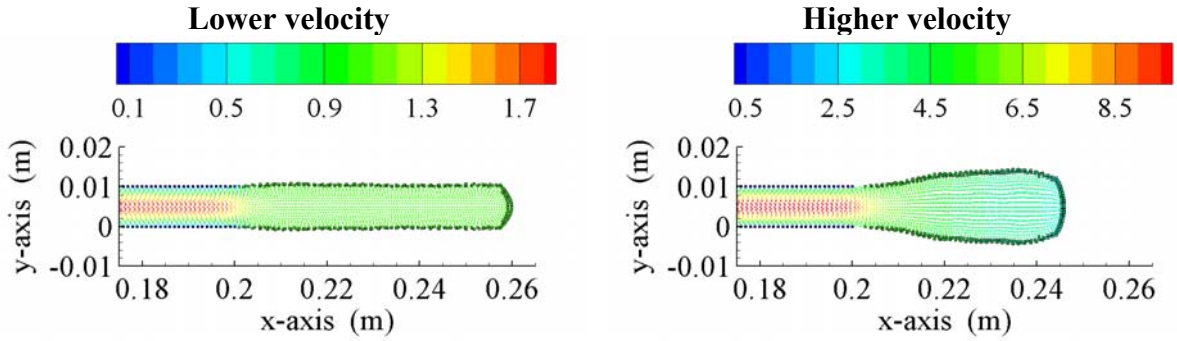

a) the magnitude of the velocity, *m/s*

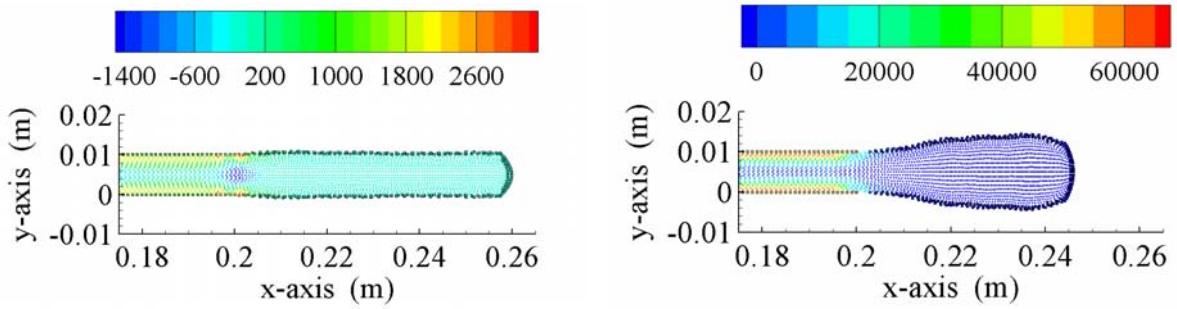

b) the normal component T_{xx} of the extra stress tensor in the *x*-direction, *Pa.*

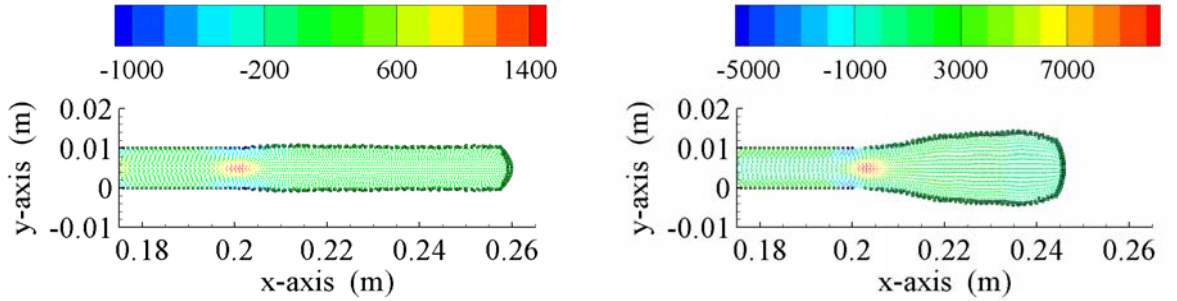

c) the normal component T_{yy} of the extra stress tensor in the y-direction, *Pa.*

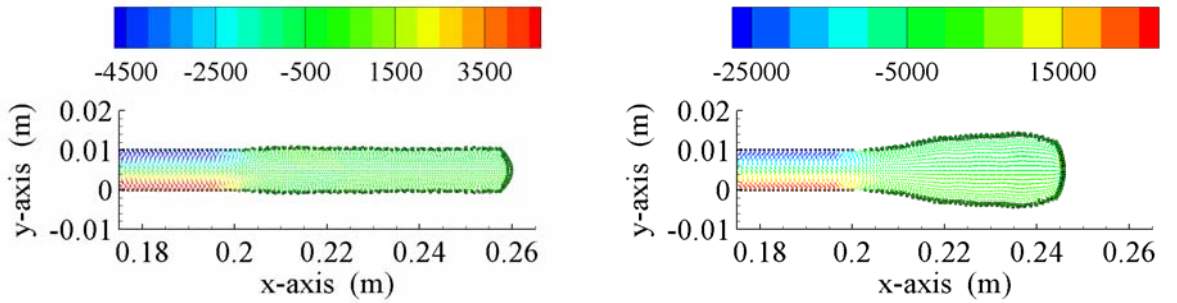

d) the shear component T_{xy} of extra stress tensor stress, *Pa.*

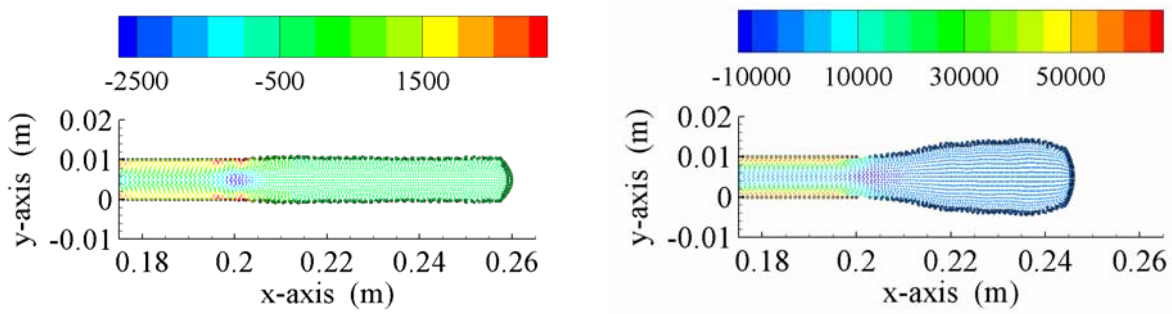

e) the first normal stress difference N_1, *Pa.*

Figure 4-11: Simulation results for two different centerline velocities within the channel.

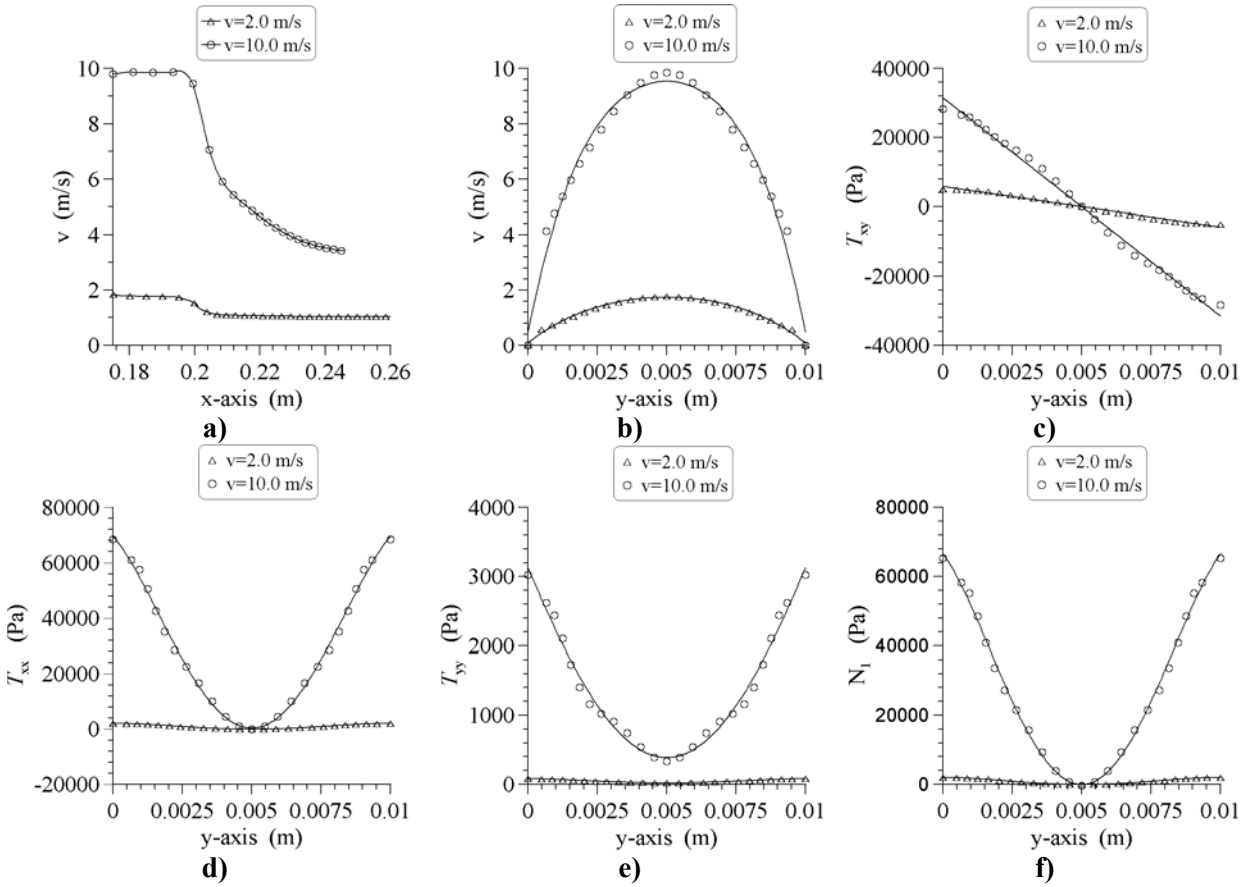

Figure 4-12: a) Magnitude of the velocity versus the axial distance, b) magnitude of the velocity as a function of channel width, c) the shear component T_{xy} of the extra stress tensor, d) the normal component T_{xx} of the extra stress tensor in the *x*-direction, e) the normal component T_{yy} of the extra stress tensor in the y-direction, and f) the first normal stress difference N_1. Results are shown for *x*= 0.185 m.

4.4.5 Deborah Number Effects on the Extrudate Swell

In order for understanding the effect of Deborah number as well as the inertial effect on the swelling mechanism, we performed two sets of simulations in which two different Re number values (Re=5 and 10) and various De numbers ranging from 0 to 0.5 are used (see Figure 4-13). Simulations parameters employed in the present study are listed in Table 4-1. Figure 4-14 summarizes the results of the simulations in terms of the swelling ratio versus Deborah number, and clearly shows that the radius of the extrudate jet increases monotonically as the value of De increases. Results in Figure 4-15 suggest that as the normal component of the extra stress tensor increases, so does the first normal stress difference, hence leading to an increase in the diameter of the extrudate in radial direction. Another interesting conclusion that can also be extracted from the given results is that as the De number increases, the extrudate swell starts at the die exit, while for smaller De numbers, it is delayed. We have also observed that the inertial force has a significant effect on the swelling diameter. Figure 4-13 also shows that the swelling obtained from simulations with the centerline velocity of 10 m/s (corresponding to Re number of 10) is greater than those computed with the centerline velocity of 5 m/s (Re=5).

It is noted that the WSPH algorithm presented here has an upper bound for achievable De number. For Reynolds number of 5 and 10, the upper bonds are 0.3, and 0.5, respectively. In simulations with De number values greater than these upper bounds, fluids particles accumulate at the die exit. As the simulation progress, local fractures in particle distribution starts forming at the channel exit, whereby terminating the simulation. It is experimentally well known that as the Deborah number increases, the polymeric fluids starts acting more solid like, thereby experiencing difficulties in its flow nature. As a result, it may experience fracture, which is widely referred to as "*melt fracture*" in the polymer processing industry. Nevertheless, it is believed that the upper bonds mentioned are not high enough to induce such a physical insight. Therefore, we conclude that these thresholds in obtainable Deborah numbers are of numerical nature. Investigating why WSPH approach has a threshold in achievable Deborah number is a subject of the future research in this area. We have also developed ISPH algorithm to study if the limitation in De number is due to SPH method or

not, and run several test cases. The preliminary outcomes of these runs have shown that one can obtain higher De numbers than those achievable with WSPH. The refined results will be published in a follow-up study which will involve the detailed comparison of the WSPH and ISPH results.

Table 4-1: Input parameters for simulations with various De and Re numbers.

$\mathrm{Re} = \rho h \mathrm{v} / \mu$ $De = \alpha_1 \mathrm{v} / \mu h$	v = 5 m/s , Re=5		v = 10 m/s , Re=10	
	$F_x^B \left(N/kg\right)$	$\alpha_1 \left(\mathrm{Pa}\, s^2\right)$	$F_x^B \left(N/kg\right)$	$\alpha_1 \left(\mathrm{Pa}\, s^2\right)$
0	4100.0	0.0	8170.0	0.0
0.02	3870.0	-4.0×10^{-4}	7410.0	-2.0×10^{-4}
0.1	2780.0	-2.0×10^{-3}	5670.0	-1.0×10^{-3}
0.2	1710.0	-4.0×10^{-3}	3720.0	-2.0×10^{-3}
0.3	1245.0	-6.0×10^{-3}	2578.0	-3.0×10^{-3}
0.4			1950.0	-4.0×10^{-3}
0.5			1549.0	-5.0×10^{-3}

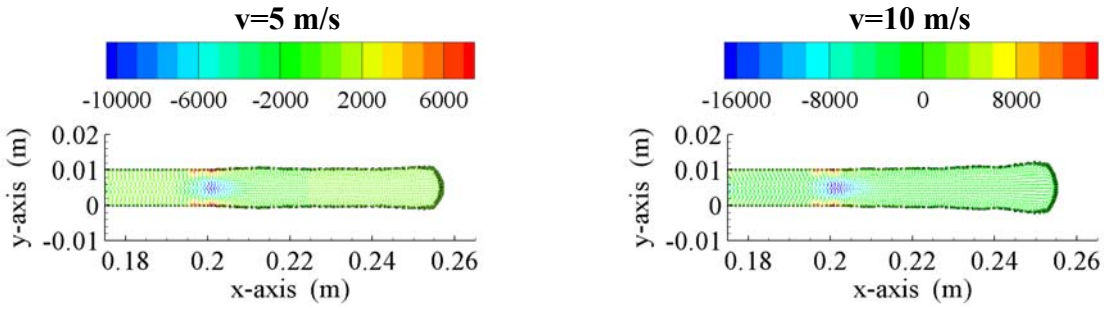

a) De=0.0

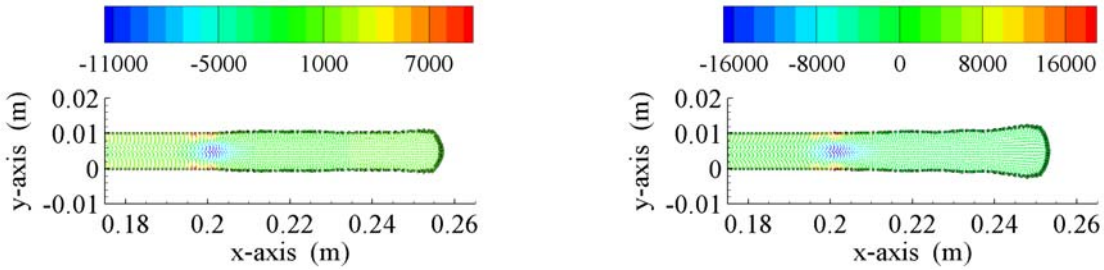

b) De=0.02

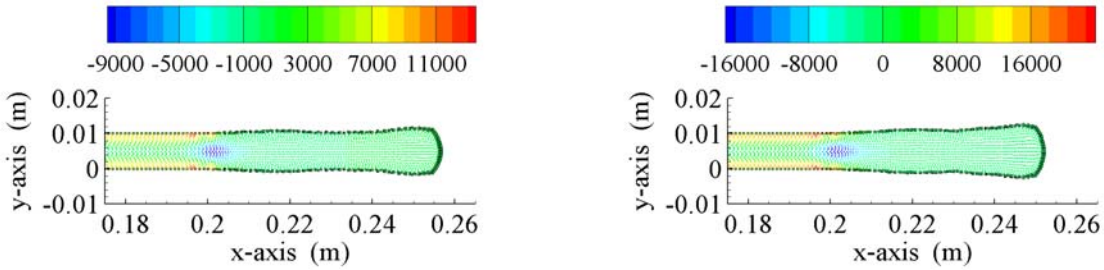

c) De=0.1

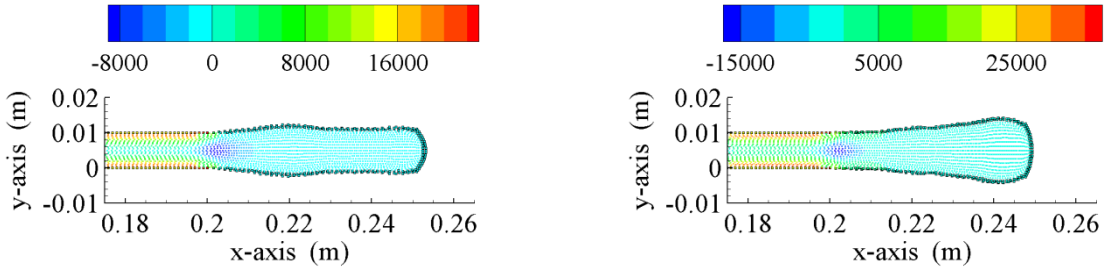

d) De=0.2

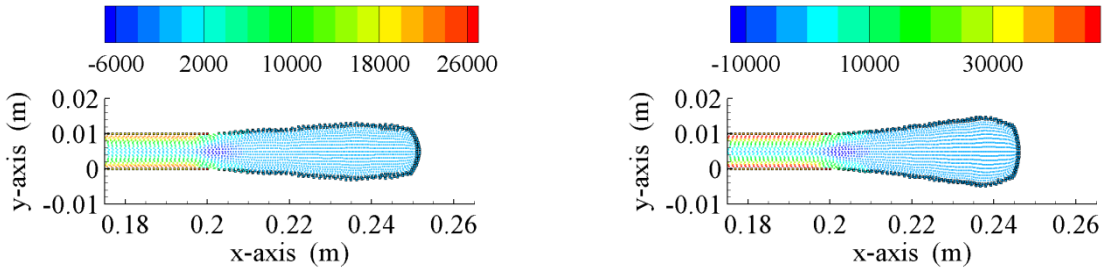

e) De=0.3

v=10 m/s

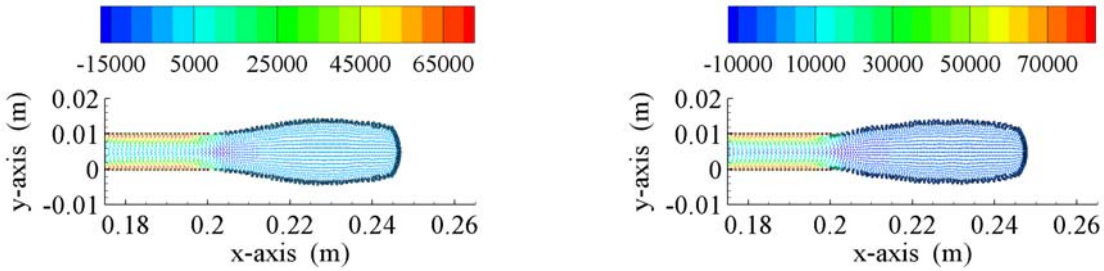

f) De=0.4 **g)** De=0.5

Figure 4-13: Particle distributions with colours denoting values of the first normal stress difference N_1 for Re numbers of 5 and 10 , and for various De numbers.

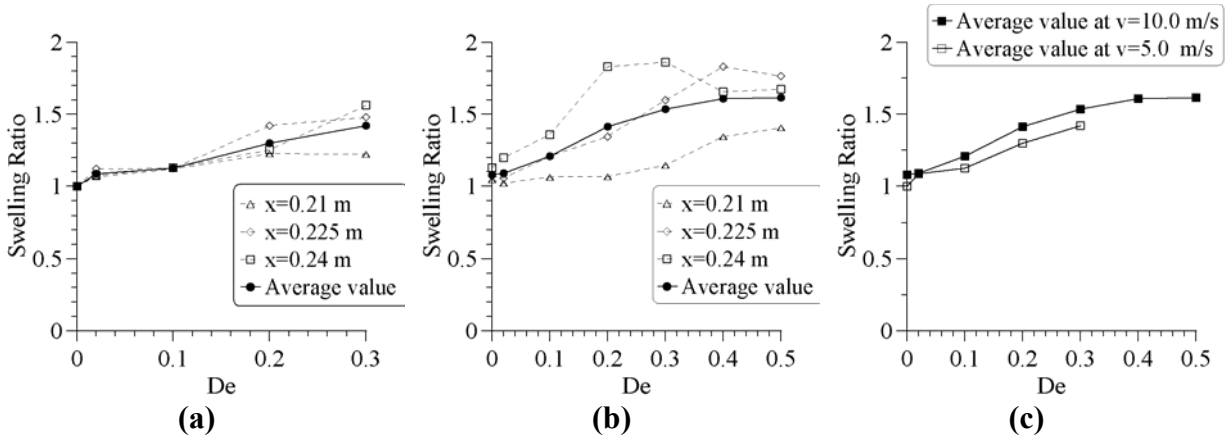

Figure 4-14: The swelling ratio at different axial positions x= 0.21, 0.23, and 0.25 m for different centerline velocities, a) v=5 m/s, b) v=10 m/s respectively, c) averaged swelling ratio for v=5 m/s and 10 m/s.

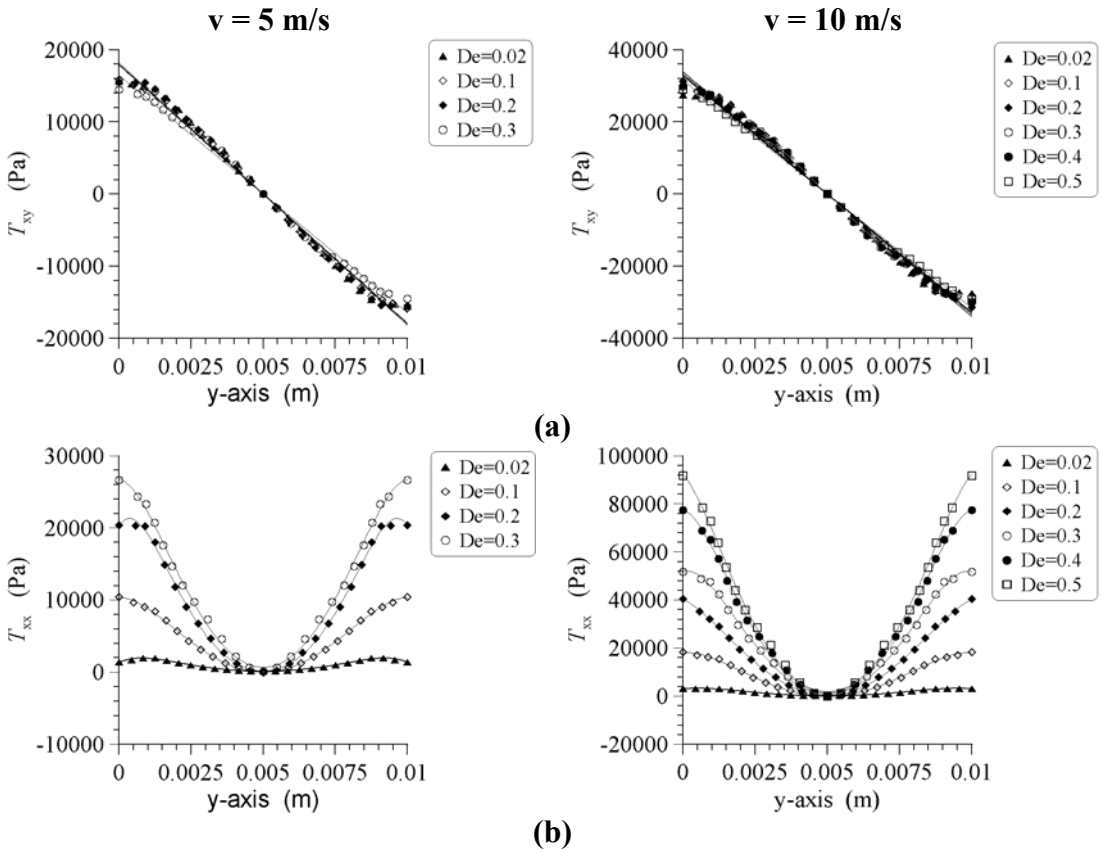

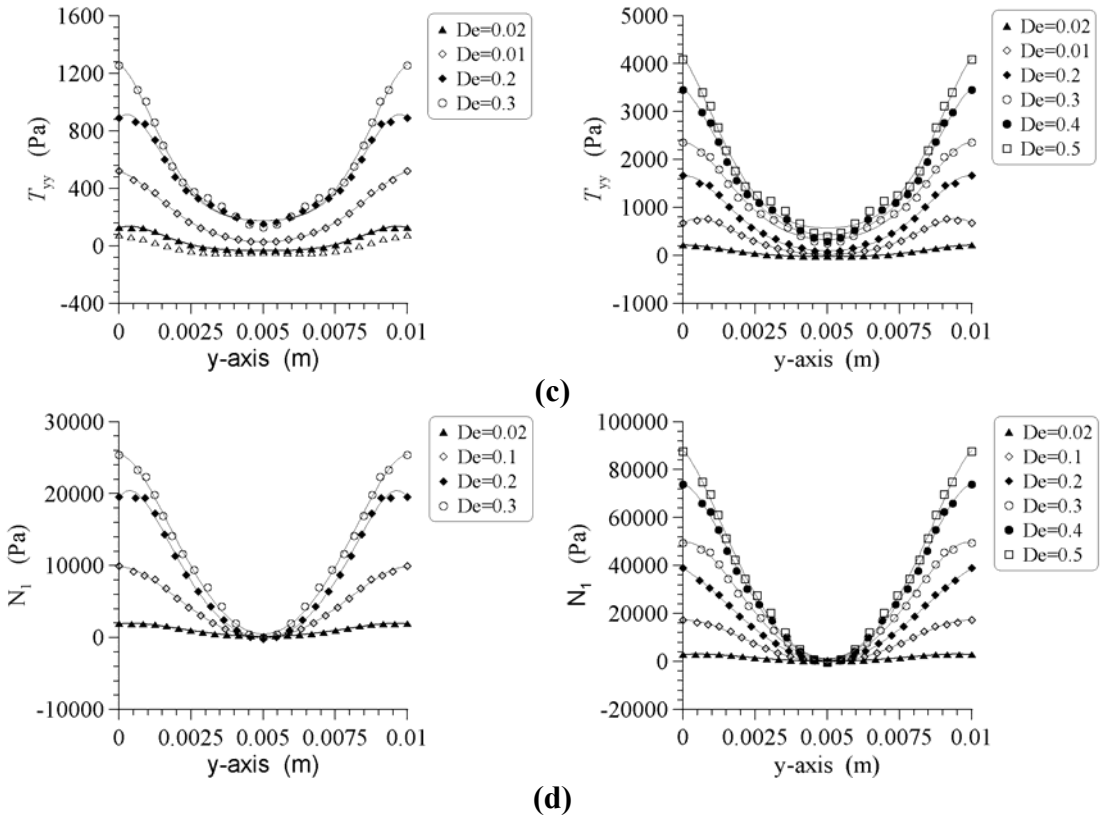

Figure 4-15: a) the shear component T_{xy} of the extra stress tensor, b) the normal component T_{xx} of the extra stress tensor in the *x*-direction, c) the normal component T_{yy} of the extra stress tensor in the y-direction, and d) the first normal stress difference N_1. Results are shown for *x*= 0.185 m.

4.4.6 WSPH Versus ISPH Algorithm

Apart from having an upper bound for obtainable De numbers, the WPSH algorithm has been proven to be very effective in modelling the extrudate swell problem. In the following, we will briefly compare the results obtained with WSPH and ISPH approaches. For both algorithms, identical simulation parameters are utilized such that the magnitude of the centerline velocity is $v \cong 6.8$ m/s, $\alpha_1 = -4.0 \times 10^{-3}$ Pa s^2, $\alpha_2 = -0.1 \times \alpha_1$, producing $De = 0.272$. One can conclude from Figure 4-16 and Figure 4-17 that results of WSPH and ISPH algorithms are in agreement except for the free surface profile. This slight discrepancy might be attributed to the difference in enforcing fluid incompressibility. As for the assessment of the average swelling

ratio, the WPSH algorithm gives an average swelling ratio of 1.362, while the ISPH algorithm produces an average swelling ratio of 1.355.

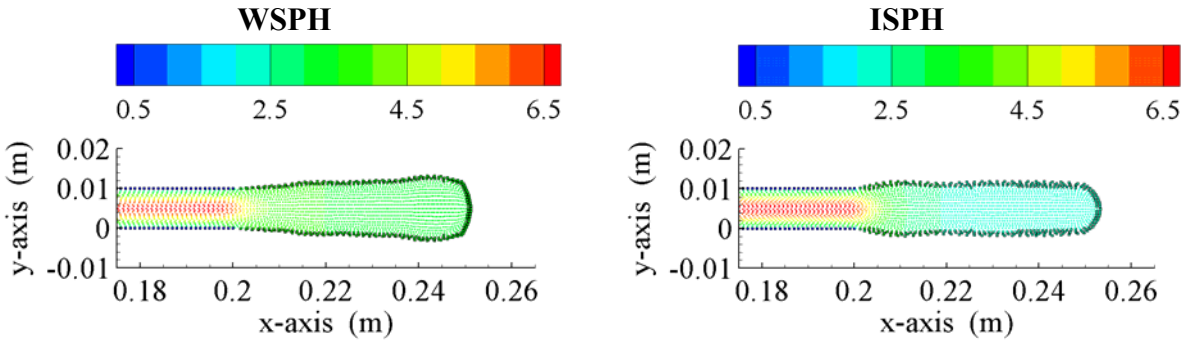

a) the magnitude of the velocity, *m/s*.

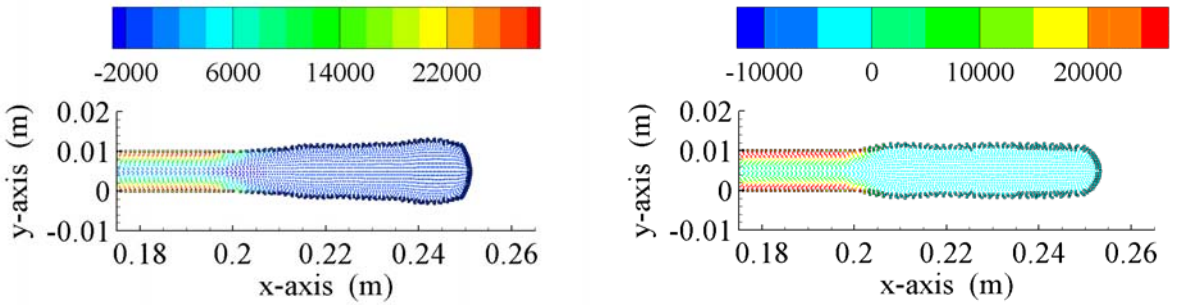

b) the normal component T_{xx} of the extra stress tensor in the *x*-direction, *Pa*.

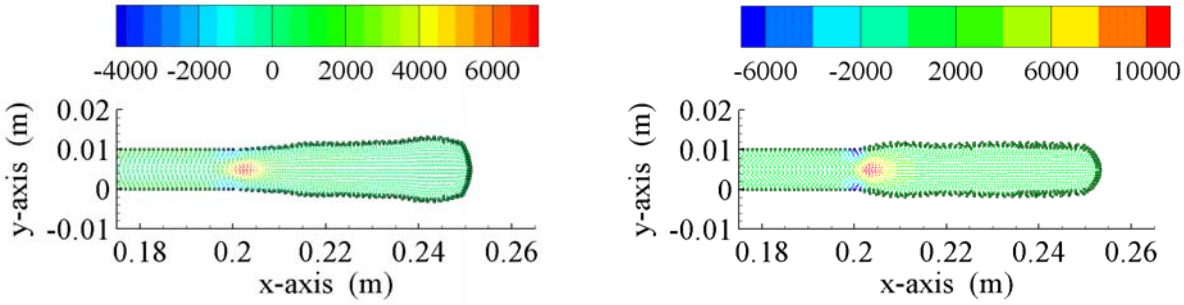

c) the normal component T_{yy} of the extra stress tensor in the y-direction, *Pa*.

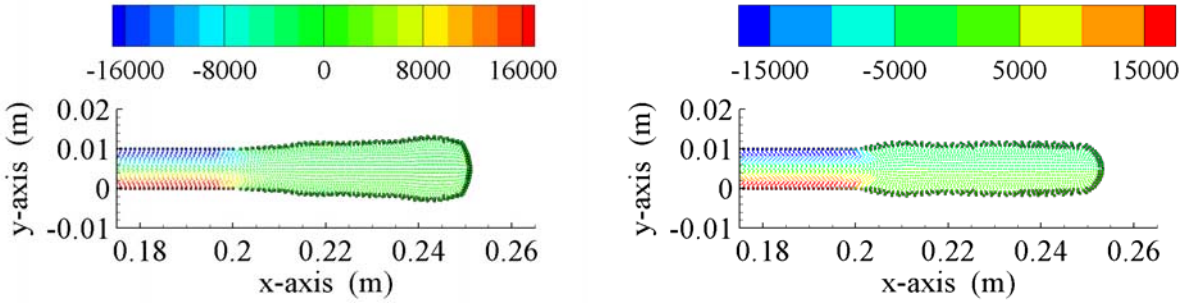

d) the shear component T_{xy} of extra stress tensor stress, *Pa*.

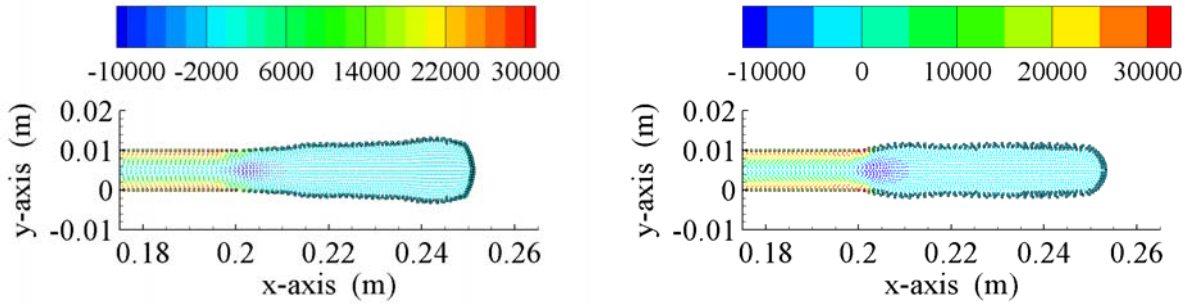

e) the first normal stress difference N_1, *Pa.*

Figure 4-16: The comparison of WSPH and ISPH algorithms.

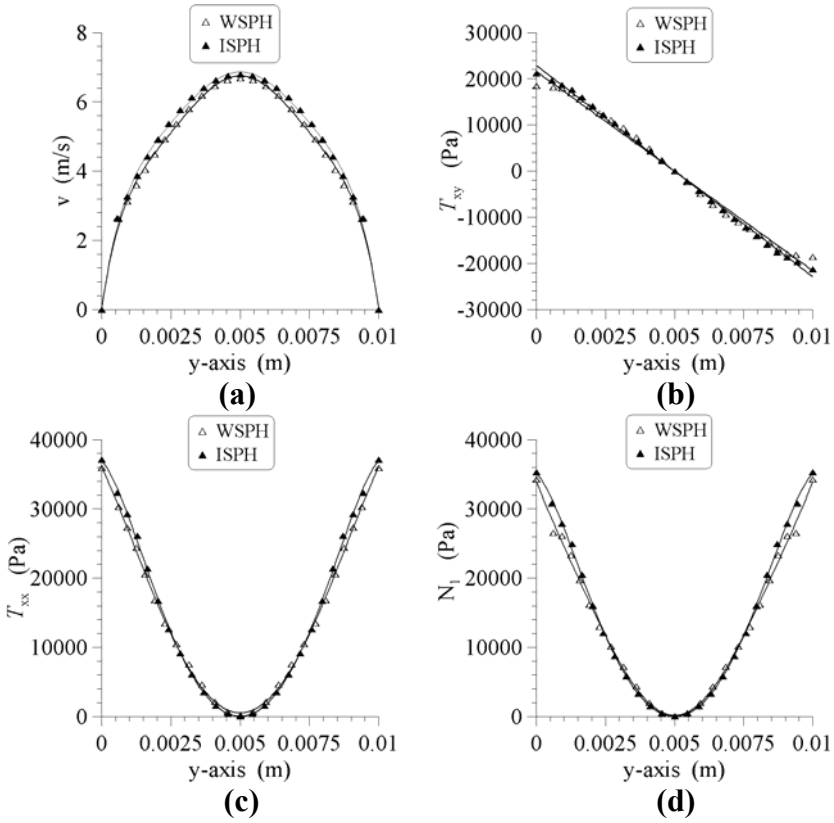

Figure 4-17: a) Magnitude of the velocity versus the axial distance, b) the shear component T_{xy} of the extra stress tensor, c) the normal component T_{xx} of the extra stress tensor in the *x*-direction, and d) the first normal stress difference N_1. Results are shown for x= 0.185 m.

CHAPTER 5

5 CONCLUDING REMARKS AND FUTURE WORK

The SPH method has proven itself to be an effective technique to model second order fluids with free surface flows as it allows the relatively easy implementation of free surface tracking, which is otherwise difficult in mesh-dependent techniques, and is able to predict swelling behaviour of the second order polymeric when extruded through a die. Thus, the SPH method can be considered as a viable and efficient alternative for modelling the extrudate swell. It is noted that the field variables and material functions predicted using Rivlin-Ericksen constitutive equation together with the contravariant components of the convected derivative of the viscous stress tensor give rise to a correct trend in swelling behaviour of polymeric fluids. In addition, it was found that the elastic stress tensor should be treated separately and computed in two steps in order to obtain correct results. The effects of various rheological and processing parameters on the swelling phenomenon have been presented such as the magnitude and sign of the first and second normal stress coefficients, velocity of flow, and Deborah number. In light of the simulation results, one can rightfully conclude that the SPH method is able to capture both swelling and contraction behaviour of a second-order polymeric fluid correctly. It has been shown that results obtained using both the WSPH and the ISPH algorithms are in agreement.

We have noted that the WSPH algorithm has a limitation in terms of the achievable Deborah number. Investigating why WSPH approach has a threshold in achievable Deborah number is a subject of the future research in this area. We have also developed ISPH algorithm to study if the limitation in De number is due to SPH method or not, and run several test cases. The preliminary outcomes of these runs have shown that one can obtain higher De numbers than

those achievable with WSPH. The refined results will be published in a follow-up study which will involve the detailed comparison of the WSPH and ISPH results. Furthermore, the developed WSPH and ISPH codes for second order viscoelastic non-Newtonian fluid will be extended to model other complicated physics in the field of polymer processing such as the modeling of elecro-spinning of single and multiphase polymeric fluids under the influence of electric field, and droplet formation of non-Newtonian fluid at the tip of a capillary tube.

REFERENCES

1. Liang Y, Oztekin A, Neti S. Dynamics of viscoelastic jets of polymeric liquid extrudate. *J. Non-Newtonian Fluid Mech.* 1999; **81**: 105–132.
2. Joseph DD, Maita JE, Chen K. Delayed die swell. *J. Non-Newtonian Fluid Mech.* 1987; **24**: 31-65.
3. Mitsoulis E, Vlachopoulos J, Mirza FA. Numerical simulation of entry and exit flows in slit dies. *Polymer Engineering and Science.* 1984; **24**: 707-715.
4. Mitsoulis E. The numerical simulation of boger fluids: a viscometric approximation approach. *Polymer Engineering and science.* 1986; **22**: 1552–1562.
5. Mitsoulis E. Three-dimensional non-newtonian computations of extrudate swell with the finite element method. 1999; **180**: 333–344.
6. Gast L, Ellingson W. Die swell measurements of second-order fluids: numerical experiments. *Int. J. Numer. Meth. Fluids.* 1999; **29**: 1–18.
7. Ahn Y-C, Ryan ME. A finite difference analysis of the extrudate swell problem. *International Journal for Numerical Methods In Fluids.* 1991; **13**: 1289-1310.
8. Tome MF, Doricio JL, Castelo A, Cuminato JA, McKee S. Solving viscoelastic free surface flows of a second-order fluid using a marker-and-cell approach. *Int. J. Numer. Meth. Fluids.* 2007; **53**: 599–627.
9. De Paulo GS, Tome MF, McKee S. A marker-and-cell approach to viscoelastic free surface flows using the PTT model. *J. Non-Newtonian Fluid Mech.* 2007; **147**: 149–174.
10. Mitsoulis E, Vlachopoulos J, Mirza FA. Simulation of vortex growth in planar entry flow of a viscoelastic fluid. *Journal of Applied Polymer Science.* 1985; **30**: 1379-1391.
11. McKee S, Tome MF, Ferreira VG, et al. Review The MAC method. *Computers & Fluids* 2008; **37**: 907–930.
12. Gingold RA, Monaghan JJ. Smooth particle hydrodynamics: theory and application to non-spherical stars. *Mon. Not. R. Astron.* 1977; **181**: 375-389.
13. Rook R, Yildiz M, Dost S. Modeling transient heat transfer using SPH and implicit time integration. *Numerical Heat Transfer.* 2007; **51** (Part B): 1–23.
14. Monaghan JJ, Kocharyan A. SPH simulation of multi-phase flow. *Computer Physics Communications.* 1995; **87**: 225-235.
15. Monaghan JJ, Huppert HE, Worster MG. Solidification using smoothed particle hydrodynamics. *Journal of Computational Physics.* 2005; **206**: 684–705.
16. Rook R, Dost S. The use of smoothed particle hydrodynamics for simulating crystal growth from solution. *International Journal of Engineering Science.* 2007; **45**: 75–93.
17. Seoa S, Min O. Axisymmetric SPH simulation of elasto-plastic contact in the low velocity impact. *Computer Physics Communications.* 2006; **175**: 583–603.

18. Shao S, Lo EYM. Incompressible SPH method for simulating newtonian and non-newtonian flows with a free surface. *Advances in Water Resources.* 2003; **26**: 787–800.
19. Fang J, Owensb RG, Tacher L, Parriaux Al. A numerical study of the SPH method for simulating transient viscoelastic free surface flows. *J. Non-Newtonian Fluid Mech.* 2006; **139**: 68–84.
20. Fang J, Parriaux A, Rentschler M, Ancey C. Improved SPH methods for simulating free surface flows of viscous fluids. *Applied Numerical Mathematics.* 2009; **59**: 251–271.
21. Morris JP, Fox PJ, Zhu Y. Modeling low Reynolds number incompressible flows using SPH. *Journal of Computational Physics.* 1997; **136**: 214–226.
22. Ellero M, Kröger M, Hess S. Viscoelastic flows studied by smoothed particle dynamics. *J. Non-Newtonian Fluid Mech.* 2002; **105**: 35–51.
23. Ellero M, Tanner RI. SPH simulations of transient viscoelastic flows at low Reynolds number. *J. Non-Newtonian Fluid Mech.* 2005; **132**: 61–72.
24. Rafiee A, Manzari MT, Hosseini M. An incompressible SPH method for simulation of unsteady viscoelastic free-surface flows. *International Journal of Non-Linear Mechanics.* 2007; **42**: 1210 –1223.
25. Massoudi M, Vaidya A. On some generalizations of the second grade fluid model. *Nonlinear Analysis: Real World Applications.* 2008; **9**: 1169 –1183.
26. Labropulu F, Xu X, Chinichian M. Unsteady stagnation point flow of a non-newtonian second-grade fluid. *Mathematics Subject Classification.* 2000; **60**: 3797-3807.
27. Osswald TA, Hernández-Ortiz JP. *Polymer Processing: Modeling and Simulation*. Hanser Gardner Publications, Inc.: USA; 2006.
28. Dunn JE, Fosdick RL. Thermodynamics, stability and boundedness of fluids of complexity 2 and fluids of second grade. *Arch. Ration. Mech. Anal.* 1974; **56**: 191–252.
29. Han CD. *Rheology and Processing of Polymeric Materials.* Vol 1. Oxford University Press, Inc.: New York; 2007.
30. Monaghan JJ. Smoothed particle hydrodynamics. *Rep. Prog. Phys.* 2005; **68** 1703–1759.
31. Monaghan JJ. Smoothed particle hydrodynamics. *Annu. Rev. Astron. Astrophys.* 1992; **30**: 543-574.
32. Liu GR, Liu MB. *Smoothed Particle Hydrodynamics: A Meshfree Particle Method*. World Scientific Publishing Co. Pte. Ltd.: Singapore; 2003.
33. Yildiz M, Rook RA, Suleman A. SPH with the multiple boundary tangent method. *Int. J. Numer. Meth. Engng.* 2009; **77**: 1416–1438.
34. Rodriguez-Paz M, Bonet J. A corrected smooth particle hydrodynamics formulation of the shallow-water equations. *Computers and Structures.* 2005; **83**: 1396–1410.
35. Cummins SJ, Rudmany M. An SPH projection method. *Journal of Computational Physics* 1999; **152**: 584–607
36. Yildiz M. *Growth of bulk SiGe single crystals by liquid phase diffusion method: experimental and computational aspects*. Vdm verlag; 2009.